Adaptive fourth-order phase field method for rock fractures using novel refinement criteria and improved data transfer operators

Feng Zhu[a], Hongxiang Tang[a,] *, Feng Liu[a], Xue Zhang[b]

[a]State Key Laboratory of Coastal and Offshore Engineering, Dalian University of Technology, 116023 Dalian, China

[b]Department of Civil Engineering and Industrial Design

University of Liverpool, Liverpool, L69 3BX, UK

* Corresponding author.

Abstract： High computing cost restricts the application of phase field models in geotechnical engineering (e.g., in blasting, oil and gas exploration, and rock landslides). To improve computational efficiency, this paper proposes an adaptive isogeometric method of the phase-field model for simulating rock fracture using a novel refinement criterion and an improved data transfer operator (HBFT). The proposed method is shown to decrease the calculation time and storage requirements by over 90% compared to the uniform refinement in most cases, and the computing time of incorporating non-equal order cells is 35.23% less than that of the equal order case. Notably: (1) the proposed refinement criterion is simple and efficient, and relies only on the 1D knot vector of the IGA to guarantee the hierarchical difference of adjacent cells.(2) the proposed HBFT only transfers the history variables in the local region to be refined, while keeping the variables in other regions unchanged; additionally, compared with the global and cell-by-cell versions in the traditional BFT, the proposed HBFT not only has the potential to avoid solving large-scale linear equations of the global version, but also alleviates, to a certain extent, the requirement of the cell-by-cell version for the full integration cell.

Keywords: Rock fracture, Phase-field model, Adaptivity, Hierarchical splines, Isogeometric analysis.

1. Introduction

Many geotechnical problems on Earth are associated to rock fractures, such as blasting (Zhu and Zhao, 2021), oil and gas exploration (Aimene et al., 2019), and rock landslides (Cheng et al., 2021; Gong et al., 2021; Li et al., 2019; van derBeek, 2021). Generally, crack initiation and propagation are the main influencing factors in these engineering problems (Goswami et al., 2020a; Wu et al., 2019). However, due to its complex mechanisms and numerous influencing factors (Ambati et al., 2014), rock fracture is usually difficult to predict accurately and often causes serious damage to property and life safety. It is thus clear that the research on rock fractures is of great significance in geotechnical engineering.

In addition to experimental studies and theoretical analyses, numerical methods are an effective means to study rock fractures, especially for those expensive or unfeasible full-scale experiments. Generally, popular approaches include, but not restricted to, discrete element method (Camones et al., 2013; Gaume et al., 2015), peridynamics (Oterkus et al., 2017; Rabczuk and Ren, 2017; Song and Silling, 2020; Zhu and Zhao, 2021), extend finite element method (Cruz et al., 2019, 2018), meshless method (Zhuang et al., 2014, 2012), and phase-field model (Borden et al., 2014; Bourdin et al., 2000; Spetz et al., 2021). Notably, (Ren et al., 2017, 2016) developed a dual-horizon peridynamics (DH-PD) formulation that not only naturally includes varying horizon sizes and completely solves the ‘ghost force’ issue, but it also allows for simulations with dual-horizon with minimal spurious wave reflection. Later on, (Rabczuk and Ren,

2017) extended it to fracture issues in granular and rock-like materials. It can simulate crack branching and coalescence without ad-hoc criteria. More information can be found in (Ren, 2021). A comparison of these methods can be found in (Wu et al., 2019). Among the aforementioned methods, the phase-field model has attracted considerable scholarly attention in recent years and is widely applied in geological engineering. For instance, zhou et al. (Zhou et al., 2018a) developed a phase-field approach for poroelastic media to simulate hydraulic fracture in the geological field. Fei and Choo (Fei and Choo, 2020) developed a modified phase field model for a common geologic shear fracture in onshore and offshore landslides. Hu et al (Hu et al., 2022) combined the material point method and the phase-field model to study slope stability under finite deformation.

However, the phase-field model also faces a series of tough challenges, such as inaccurate location of the crack tip and high computational costs (Wu et al., 2019). In this paper, we mainly focus on the latter issue. Currently, the most efficient solutions include, but are not restricted to, parallel computing (Samaniego et al., 2021), double mesh techniques (Goswami et al., 2019; Zhu et al., 2022), and adaptive remeshing technique (Goswami et al., 2020b; Li et al., 2022).

In light of the above, and inspired by the pioneering work of (Garau and Vázquez, 2018; Goswami et al., 2020b, 2019; Hennig et al., 2018) et al., this study develops an adaptive isogeometric method of the fourth-order phase field model for simulating rock fracture using a novel refinement criterion and an improved data transfer operator. Notably, the proposed adaptive phase-field method, although implemented in simple

hierarchical splines (i.e., SHB-splines), can be directly extended to all kinds of hierarchical splines that conform to the definition in (Giannelli et al., 2014), e.g., standard hierarchical splines (Vuong et al., 2011) and truncated hierarchical splines (i.e., THB-splines) (Giannelli et al., 2012). In brief, the contribution of this work can be summarized in the following three points:

(1) An adaptive isogeometric method of the fourth-order phase-field model is developed for simulating rock fracture in geotechnical engineering. The proposed method is shown to reduce the computing time and storage requirements by more than 90% compared to the uniform refinement in most cases.

(2) A novel refinement criterion, termed as the cling film refinement criterion, is proposed. The proposed criterion is easy to implement and reduces the number of computing cells.

(3) An improved data transfer operator, denoted as HBFT, is proposed for history variables at integration points. Compared with the global and cell-by-cell versions in the traditional BFT, HBFT not only has the potential to avoid solving large-scale linear equations of the global version, but also alleviates, to a certian extent, the requirement of the cell-by-cell version for the full integration cell. Additionally, HBFT only transfers the history variables in the local region to be refined, while keeping those within the remaining regions unchanged, as displayed in Fig. 8.

The remaining sections are organized as follows. In Section 2, we present the concepts of the phase-field model. In Section 3, we provide the implementation details of the proposed adaptive phase-field approach. Additionally, this section also presents

the novel refinement criterion and the improved data transfer operator. Section 4 then illustrates the performance of the proposed method by numerical examples. The final conclusions are given in Section 5.

2. Phase-field modelling for fracture

The phase-field model seeks to simultaneously solve for the elastic field and crack region by energy minimization, thereby eliminating ad-hoc criteria and avoiding the capture of fracture surface topology. In brief, The total energy Φ of the phase field model can be denoted as

$$\Phi := \Phi_b + \Phi_c - \Phi_{external} \tag{1}$$

Where Φ_b is the volume energy, Φ_c is the fracture energy, and $\Phi_{external}$ is the external potential energy. Among then, Φ_b and Φ_c can be formulated as

$$\Phi_{\mathrm{c}} = \int_{\Omega} G_c \, \Gamma_{\phi,4} d\Omega \tag{2}$$

$$\Phi_{\mathrm{b}} = \int_{\Omega} g_2(\phi) \, \Phi_{elastic} d\Omega \tag{3}$$

where G_{C} is the critical energy release rate, ϕ is the damage variable (or phase field), and $\Phi_{elastic}$ is the elastic strain energy density. Besides, the fourth-order crack surface density functional $\Gamma_{\phi,4}$ (Borden et al., 2014) and the second-order stress degradation function $g_2(\phi)$ can be written as follows:

$$\Gamma_{\phi,4} = \frac{\phi^2}{2L_{\mathrm{c}}} + \frac{L_{\mathrm{c}}}{4}\left(\nabla(\phi)\right)^2 + \frac{{L_{\mathrm{c}}}^3}{32}(\Delta\phi)^2 \tag{4}$$

$$g_2(\phi) = (1-\phi)^2 \tag{5}$$

where L_c is the length-scale parameter . As L_c infinitely approximates to 0, a sharp cracked surface will be regained. Fig. 1 presents a schematic diagram of a diffuse crack obtained using the phase-field model

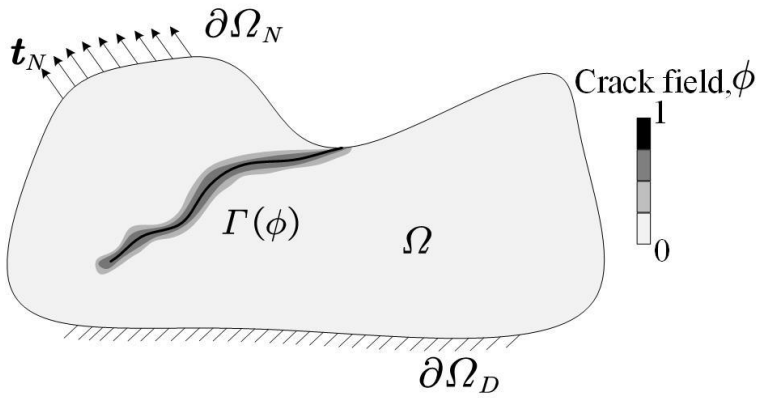

Fig. 1. Schematic diagram of diffuse cracks

2.1 Energy decomposition

To address the potential unphysical crack patterns in compression stress, a common solution (Miehe et al., 2010) is to split the elastic strain energy density $\Phi_{elastic}$ into a corresponding tension component ${\Phi_{elastic}}^{+}$ and a compression component ${\Phi_{elastic}}^{-}$.

$$ {\Phi_{elastic}}^{\pm} = \frac{\lambda\langle tr[\boldsymbol{\varepsilon}]\rangle_{\pm}^{2}}{2} + \mu tr\left[\boldsymbol{\varepsilon}_{\pm}^{2}\right] \tag{6} $$

where λ and μ are the $lamé$ coefficients, and $\boldsymbol{\varepsilon}_{\pm}$ can be defined as

$$ \boldsymbol{\varepsilon}_{\pm} = \sum_{I=1}^{3} \langle \varepsilon_I \rangle_{\pm} \boldsymbol{n}_I \otimes \boldsymbol{n}_I \tag{7} $$

where $\varepsilon_I$and $\boldsymbol{n}_I$ are the eigenvalues and eigenvectors of the strain tensor, respectively, and the operator $\langle x\rangle_{\pm}$ can be formulated as

$$\langle x\rangle_{\pm} := \frac{(x \pm |x|)}{2} \tag{8}$$

Hence, the stored bulk energy Φ_b, i.e., Eq. (3), can be reformulated as

$$\Phi_b = \int_{\Omega} \left(g_2(\phi) {\Phi_{elastic}}^{+} + {\Phi_{elastic}}^{-} \right) d\Omega \tag{9}$$

As seen, $g_2(\phi)$ acts only on ${\Phi_{elastic}}^{+}$ in Eq. (9), which indicates that only the tension component is degraded, while the compression component is kept invariant.

2.2 Hybrid model and staggered scheme

Simulating crack propagation using the phase-field model involves solving for the vector-valued displacement field $\boldsymbol{u}$ and the scalar-valued damage field ϕ. The commonly used method is the staggered scheme. Although it is capable of handling unstable fracture extension, it is computationally expensive. Ambati et al. (Ambati et al., 2014) therefore proposed a hybrid-staggered scheme, which dramatically reduces the calculation costs with the same robustness.

In the hybrid-staggered scheme, the displacement field is free from energy decomposition, meaning that ${\Phi_{elastic}}^{-} = 0$, $\Phi_{elastic} = {\Phi_{elastic}}^{+}$, and Eq. (9) is rewritten as $\Phi_b = \int_{\Omega} g_2(\phi) \Phi_{elastic}\, d\Omega$, thus the equilibrium equation is formulated as follows

$$-\nabla \cdot g_2(\phi)\boldsymbol{\sigma} = \boldsymbol{f} \tag{10}$$

where $\boldsymbol{\sigma} = \frac{\partial \Phi_{elastic}(\boldsymbol{\varepsilon})}{\partial \boldsymbol{\varepsilon}}$. And the evolution equation for the damage field ϕ is written as

$$G_{\mathrm{c}} \left[\frac{\phi}{L_{\mathrm{c}}} - \frac{L_{\mathrm{c}}}{2} |\nabla \phi|^2 + \frac{{L_{\mathrm{c}}}^3}{16} \triangle^2 \phi \right] = -{g_2}'(\phi) H(\boldsymbol{x},t) \tag{11}$$

where $H(\boldsymbol{x},t) = \max_{t\in[t_0,t_n]} \Phi_{elastic}{}^{+}\left(\boldsymbol{\varepsilon}(\boldsymbol{x},t)\right)$ is the history field variable for preventing crack healing.

3. Adaptive phase-field approach with simplified hierarchical splines

3.1 Simplified hierarchical splines

To define the simplified hierarchical splines (Garau and Vázquez, 2018), we first consider a given sequence B-spline space $\{\mathcal{S}_l\}_{l\in\mathbb{N}_0}$ of depth n such that

$$\mathcal{S}_0 \subset \mathcal{S}_1 \subset \mathcal{S}_2 \ldots \subset \mathcal{S}_n \tag{1}$$

which are defined by knot vectors and orders. For any spline space $\mathcal{S}_l$, $\mathcal{B}_l$ denotes its B-spline basis, N_l indicates its space dimension, and $\mathcal{Q}_l$ represents its Cartesian mesh in parametric space. If $Q_l \in \mathcal{Q}_l$, then Q_l is a cell of level l. Additionally, for any $Q_{l+1} \in \mathcal{Q}_{l+1}$, if $Q_{l+1} \subset Q_l$, we say that Q_l is a parent of Q_{l+1}, and abbreviate it as

$$Q_l = \mathcal{P}(Q_{l+1}), \qquad if\, Q_{l+1} \subset Q_l \tag{13}$$

Notably, in achieving local refinement, a frequently utilized property is the two-scale relation as illustrated in Eq. (14), i.e., B-splines of level l can be expressed as a linear combination of B-splines of level $l+1$ together with non-negative coefficients $c_{k,l+1} \geqslant 0$.

$$\beta_{i,l} = \sum_{k=1}^{N_{l+1}} c_{k,l+1}\left(\beta_{i,l}\right)\beta_{k,l+1}, \forall \beta_{i,l} \in \mathcal{B}_l, \tag{14}$$

However, due to the local support of the B-splines, there are only a small number of coefficients in Eq. (14) that satisfy $c_{k,l+1} \neq 0$. If $c_{k,l+1}(\beta_{i,l}) \neq 0$, then its corresponding function, $\beta_{k,l+1}$, is termed as a child of $\beta_{i,l}$, and the set of children of

$\beta_{i,l}$ is denoted by $\mathcal{C}_{fun}(\beta_{i,l}) \subset \mathcal{B}_{l+1}$. And, further, the B-splines of two adjacent levels have the following relationship

$$\mathcal{B}_l = C_l^{l+1}\mathcal{B}_{l+1} \tag{15}$$

where the matrix C_l^{l+1} has the following form

$$\left(C_l^{l+1}\right)_{ki} = c_{k,l+1}(\beta_{i,l}), \quad for\ \ i = 1, \dots, N_l, k = 1, \dots, N_{l+1} \tag{16}$$

And the B-splines of any two levels can be associated by applying the matrix C_l^{l+1} successively, i.e., via $C_l^{l+m} = C_{l+m-1}^{l+m} \cdots C_{l+1}^{l+2} C_l^{l+1}$. In addition, we define the set $\boldsymbol{\Omega}_n := \{\Omega_0, \Omega_1, \Omega_2, \dots, \Omega_n\}$ as a hierarchical subdomain of depth n if

$$\hat{\Omega} = \Omega_0 \supset \cdots \supset \Omega_{n-1} \supset \Omega_n = \emptyset, \tag{17}$$

and each subdomain Ω_l is the union of cells of level $l-1$.

According to the above defined $\{\mathcal{S}_l\}_{l\in\mathbb{N}_0}$, $\{\mathcal{B}_l\}_{l\in\mathbb{N}_0}$ and $\boldsymbol{\Omega}_n$, the simplified hierarchical basis $\widetilde{\mathcal{H}} := \widetilde{\mathcal{H}}_{n-1}$ proposed in (Buffa and Garau, 2017) can be derived from the following recursive formulation (18).

$$\begin{cases} \widetilde{\mathcal{H}}_0 := \mathcal{B}_0 \\ \widetilde{\mathcal{H}}_{l+1} := \{\beta \in \widetilde{\mathcal{H}}_l | supp\beta \not\subset \Omega_{l+1}\} \cup \bigcup\limits_{\substack{\beta\in\widetilde{\mathcal{H}}_l \\ supp\beta\subset\Omega_{l+1}}} \mathcal{C}(\beta), l = 0, \dots, n-2. \end{cases} \tag{18}$$

And the underlying hierarchical mesh $\mathcal{Q}$ corresponding to the hierarchical basis $\widetilde{\mathcal{H}}$ can be obtained from Eq. (19).

$$\mathcal{Q} := \bigcup_{l=0}^{n-1} \{Q \in \mathcal{Q}_l | Q \subset \Omega_l \wedge Q \not\subset \Omega_{l+1}\}. \tag{19}$$

In addition, Fig. 2 provides an example of quadratic simplified hierarchical splines containing two levels of subdomains.

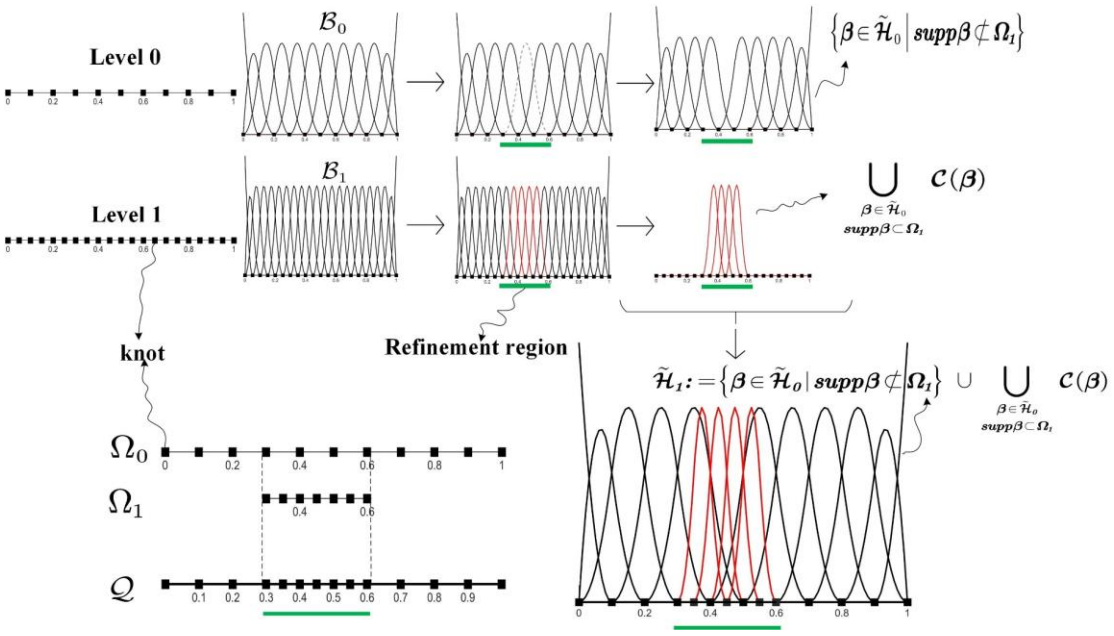

Fig. 2. An example of quadratic simplified hierarchical splines where the subdomain hierarchy consists of two levels.

3.2 Spatial discretization and matrix assembly

The variational formulation of the phase-field model is written as:

$$\int_{\Omega} \{\boldsymbol{\sigma}\delta\boldsymbol{\varepsilon} - \boldsymbol{b}\cdot\delta\boldsymbol{u}\}\, d\Omega - \int_{\partial\Omega_{\mathrm{N}}} \boldsymbol{t}_{\mathrm{N}} \cdot \delta\boldsymbol{u} d\Omega_{\mathrm{N}} = 0 \tag{20}$$

$$\int_{\Omega} G_{\mathrm{c}} \left[\frac{1}{L_{\mathrm{c}}}\phi\delta\phi + \frac{L_{\mathrm{c}}}{2}\nabla\phi\cdot\nabla\delta\phi + \frac{L_{\mathrm{c}}^{3}}{16}\triangle\phi\cdot\triangle\delta\phi\right] + g'(\phi)H(x,t)\delta\phi d\Omega = 0 \tag{21}$$

Utilizing the simplified hierarchical basis $\tilde{\beta} \in \widetilde{\mathcal{H}}_l$, the displacement increment $\boldsymbol{u}$ and the damage increment ϕ can be represented as

$$\boldsymbol{u} = \sum_{i=1}^{m} \tilde{\beta}_i^{\mathbf{u}}\, \boldsymbol{u_i}, \qquad \phi = \sum_{j=1}^{n} \tilde{\beta}_j^{\phi}\, \phi_j \tag{22}$$

where $\tilde{\beta}_i^{\mathbf{u}}$ and $\boldsymbol{u_i}$ can be denoted as

$$\tilde{\beta}_i^{\mathbf{u}} = \begin{bmatrix} \tilde{\beta}_i & 0 \\ 0 & \tilde{\beta}_i \end{bmatrix}, \qquad \boldsymbol{u_i} = \begin{bmatrix} u_x \\ u_y \end{bmatrix} \tag{23}$$

Finally, the following linear equations can be obtained after applying the Newton-Raphson method

$$\begin{bmatrix} K^{uu} & 0 \\ 0 & K^{\phi\phi} \end{bmatrix} \begin{Bmatrix} \Delta \boldsymbol{u} \\ \Delta \phi \end{Bmatrix} = \begin{Bmatrix} F^{u} \\ F^{\phi} \end{Bmatrix} \tag{24}$$

Among them, K^{uu} and $K^{\phi\phi}$ are written as follows:

$$K_{ir}^{uu} = \int_{\Omega} g(\phi)(B_i^u)^{\mathrm{T}} C_{\mathrm{e}} B_r^u d\Omega \tag{25}$$

$$K_{js}^{\phi\phi} = \int_{\Omega} \left\{ G_{\mathrm{c}} \left[\left(\frac{1}{L_{\mathrm{c}}} + 2H(x,t) \right) \tilde{\beta}_j \tilde{\beta}_s + \frac{L_{\mathrm{c}}}{2} \left(B_j^{\phi} \right)^{\mathrm{T}} B_s^{\phi} + \frac{L_{\mathrm{c}}^{3}}{16} D_j^{\phi} D_s^{\phi} \right] \right\} d\Omega \tag{26}$$

where C_{e} is the elastic stiffness matrix, and B_i^u, B_j^{ϕ} and D_j^{ϕ} respectively have the following forms

$$\boldsymbol{B}_i^{\mathbf{u}} = \begin{bmatrix} \tilde{\beta}_{i,x} & 0 \\ 0 & \tilde{\beta}_{i,y} \\ \tilde{\beta}_{i,y} & \tilde{\beta}_{i,x} \end{bmatrix}, \quad \boldsymbol{B}_j^{\phi} = \begin{bmatrix} \tilde{\beta}_{j,x} \\ \tilde{\beta}_{j,y} \end{bmatrix}, \quad \boldsymbol{D}_j^{\phi} = \tilde{\beta}_{j,xx} + \tilde{\beta}_{j,yy} \tag{27}$$

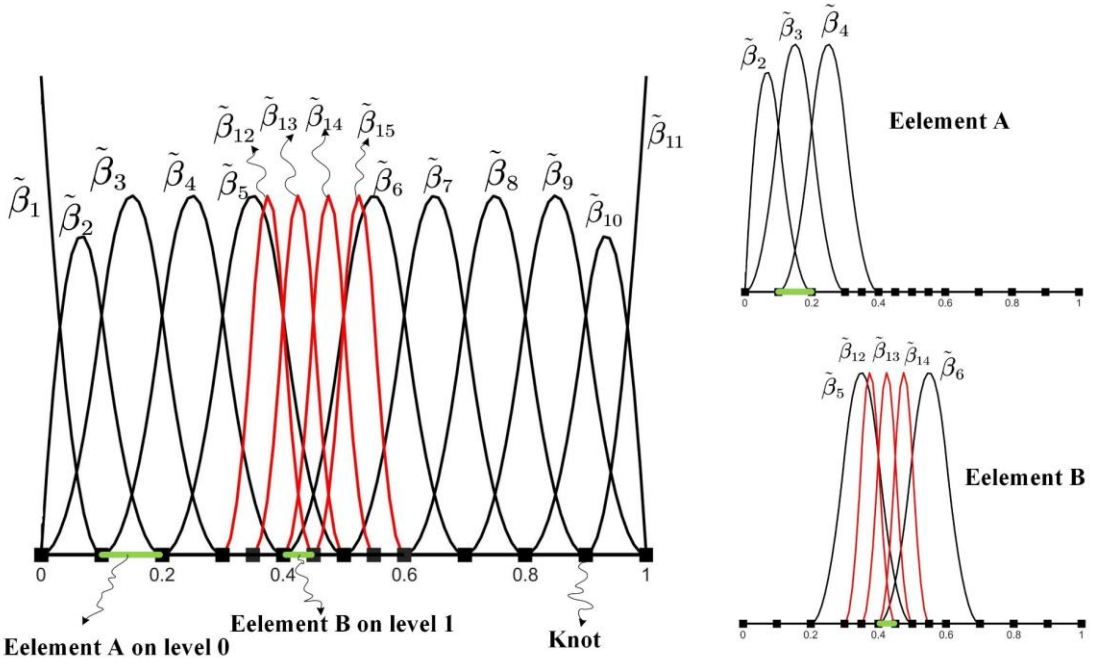

Fig. 3. Shape functions acting on elements of different levels

As illustrated in Fig. 3, the shape functions acting on the element are likely to be from different levels, and the number of shape functions for each element is not constant. Thus, one key issue to be addressed when implementing local refinement using simplified hierarchical splines is matrix assembly. The authors adopted the method proposed in (Bornemann and Cirak, 2013; Schillinger et al., 2012), which is widely used, as in (Garau and Vázquez, 2018; Hennig et al., 2016). For convenience, we take the first term in Eq. (26), i.e., $K^{term1}=\int_{\Omega}\left[G_{\mathrm{c}}\left(\frac{1}{L_{\mathrm{c}}}+2H(x,t)\right)\tilde{\beta}_j\tilde{\beta}_s\right]d\Omega$, as an example to introduce this method.

First, assume that the simplified hierarchical spline basis $\widetilde{\mathcal{H}}$ is:

$$\widetilde{\mathcal{H}}=\{\tilde{\beta}_1,\tilde{\beta}_2,\cdots,\tilde{\beta}_n\} \tag{28}$$

For any m, $1\leqslant m\leqslant n$, a unique integer k_m and l_m exists such that $\tilde{\beta}_m=\beta_{k_m,l_m}$. We similarly assume that the functions in $\widetilde{\mathcal{H}}$ are firstly ordered by level and secondly in each level with the same ordering as $\mathcal{B}_l$. Then, a component of the matrix K^{term1} are expressed as

$$K_{js}^{term1}=\int_{\Omega}A_{gauss}\tilde{\beta}_j\,\tilde{\beta}_s=\int_{q\in Q}A_{gauss}\tilde{\beta}_j\,\tilde{\beta}_s=\sum_{l=\max\{l_j,l_s\}}^{n-1}\sum_{q_l\in(Q_l\cap Q)}\int_{q_l}A_{gauss}\tilde{\beta}_j\,\tilde{\beta}_s\,d\Omega \tag{29}$$

where A_{js} is

$$A_{gauss}=G_{\mathrm{c}}\left(\frac{1}{L_{\mathrm{c}}}+2H(x,t)\right) \tag{30}$$

According to the two-scale relation in Eq. (14), i.e., for any β_{l_m} with $l_m<l$, it can eventually be expressed as a linear combination of l-level B-splines. Thus, Eq. (29) can be rewritten as

$$K_{js}^{term1}=\sum_{l=\max\{l_j,l_s\}}^{n-1}\sum_{w=1}^{N_l}\sum_{w'=1}^{N_l}c_{wj}^{l}\left(\sum_{q_l\in(Q_l\cap Q)}\int_{q_l}A_{gauss}\beta_{w,l}\,\beta_{w',l}\right)c_{w's}^{l}\,d\Omega \tag{31}$$

In matrix form, Eq. (31) can be formulated as

$$K_{js}^{term1}=\sum_{l=\max\{l_j,l_s\}}^{n-1}\left(\hat{c}_j^l\right)^T K_l^{term1}\hat{c}_s^l \tag{32}$$

where $\hat{c}_j^l$ and K_l^{term1} are, respectively,

$$\hat{c}_j^l:=\left[c_{1,j}^l,c_{2,j}^l,\cdots,c_{N_l,j}^l\right]^T \tag{33}$$

$$(K_l^{term1})_{ww'}=\sum_{q_l\in(Q_l\cap Q)}\int_{q_l}\left(A_{gauss}\beta_{w,l}\beta_{w',l}\right)dq_l \tag{34}$$

Further, we can get the global matrix in the following form

$$K^{term1}=\sum_{l=0}^{n-1}\left[\hat{C}_l\ \ \mathbf{0}\right]^T K_l\left[\hat{C}_l\ \ \mathbf{0}\right] \tag{35}$$

where $\hat{C}_l$ is obtained from the following recursive formula

$$\begin{cases}\hat{C}_0=J_0,\\ \hat{C}_{l+1}=\left[C_l^{l+1}\hat{C}_l,\ J_{l+1}\right], \quad for\ \ l=0,\dots,n-2.\end{cases} \tag{36}$$

where J_{l+1} refers to the inclusion of $\mathcal{H}_l^A:=\left\{\tilde{\beta}_i\middle|\tilde{\beta}_i\in\left(\widetilde{\mathcal{H}}\cap\mathcal{B}_{l+1}\right)\right\}$ into the tensor basis of the $l+1$ level, i.e., $\mathcal{B}_{l+1}$,. For more details, please refer to (Bornemann and Cirak, 2013; Hennig et al., 2016; Schillinger et al., 2012) and the references therein.

3.3 Adaptive h-refinement scheme

As with adaptive FEA, the adaptive isogeometric analysis of the phase-field model mainly includes the following three steps in any one iteration of each incremental step.

a) Solve the boundary value problem.

b) Mark elements according to the solution in (a) and the adopted refinement criterion.

c) Generate the refined hierachical mesh $\mathcal{Q}$ and refined hierarchical basis $\widetilde{\mathcal{H}}$ using the marked elements in (b), and perform data transfer between the old and new meshes.

Among them, the refinement criterion and data transfer operator are crucial aspects in adaptive analysis. Therefore, these contents will be further explained in the remainder of this section.

3.3.1 A novel refinement criterion

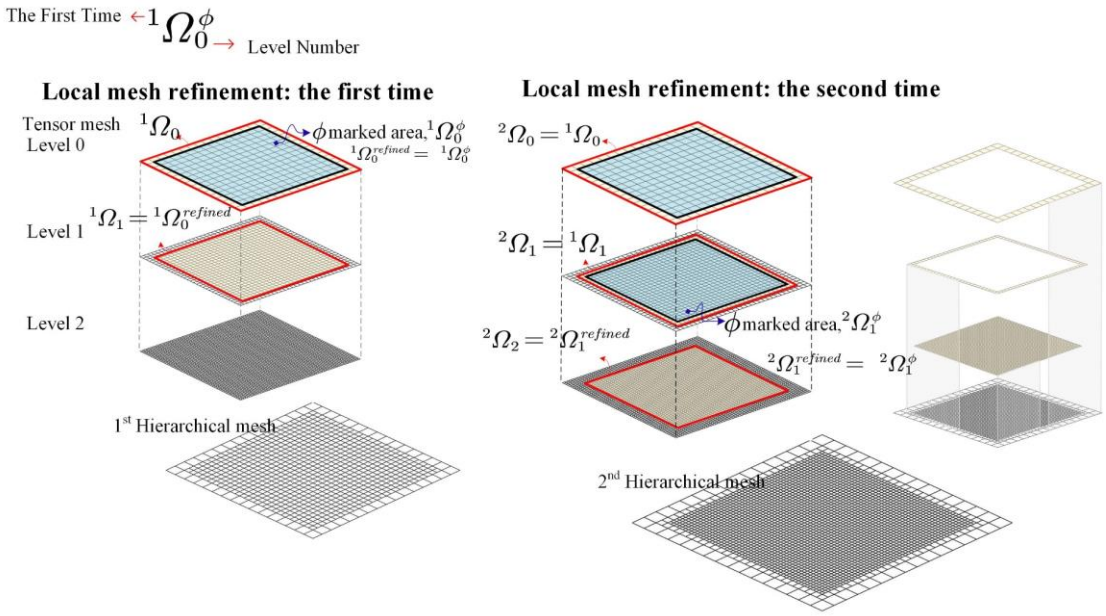

Fig. 4. A qualified hierarchical mesh with three levels (the level difference between adjacent cells is less than or equal to 1)

The commonly used refinement criteria in adaptive phase-field analysis include, but are not limited to, physics based refinement criteria (Hirshikesh et al., 2021) and damage variables ϕ (Goswami et al., 2019), etc. Among them, the damage variable ϕ is widely used due to its simplicity. However, this criterion fails to ensure that the

hierarchical difference between adjacent cells is less than or equal to 1, thus potentially producing unphysical numerical results, as depicted in Figs. 19 and 20. (As seen in Fig. 4, the number 1 in the upper left corner of ${}^{1}\Omega_0^{\phi}$ represents the first time local refinement. However, it is often ignored (i.e., Ω_0^{ϕ}) when representing the current local refinement, as long as it does not cause confusion.) A feasible and frequently applied technique is: for any ϕ -marked cell $Q_{ilevel}^{\phi} \in \mathcal{Q}_{ilevel}^{\phi}$ (i.e., $\mathcal{Q}_{ilevel}^{\phi} = \{Q | Q \in \mathcal{Q} \wedge Q \subset \Omega_{ilevel}^{\phi}\}$) in level $ilevel$, first calculate its parent cell $\mathcal{P}(Q_{ilevel}^{\phi})$ in level $ilevel-1$; secondly, in the tensor mesh of level $ilevel-1$, check whether the adjacent cells of that parent cell are active cells. If they are active cells, then mark them as cells to be refined in level $ilevel-1$. Although the method is concise, it requires checking each cell in a level-by-level, cell-by-cell manner, even for a qualified hierarchical mesh as illustrated in Fig. 4. As a result, the method is bound to waste a certain amount of computing resources, especially in 3D problems.

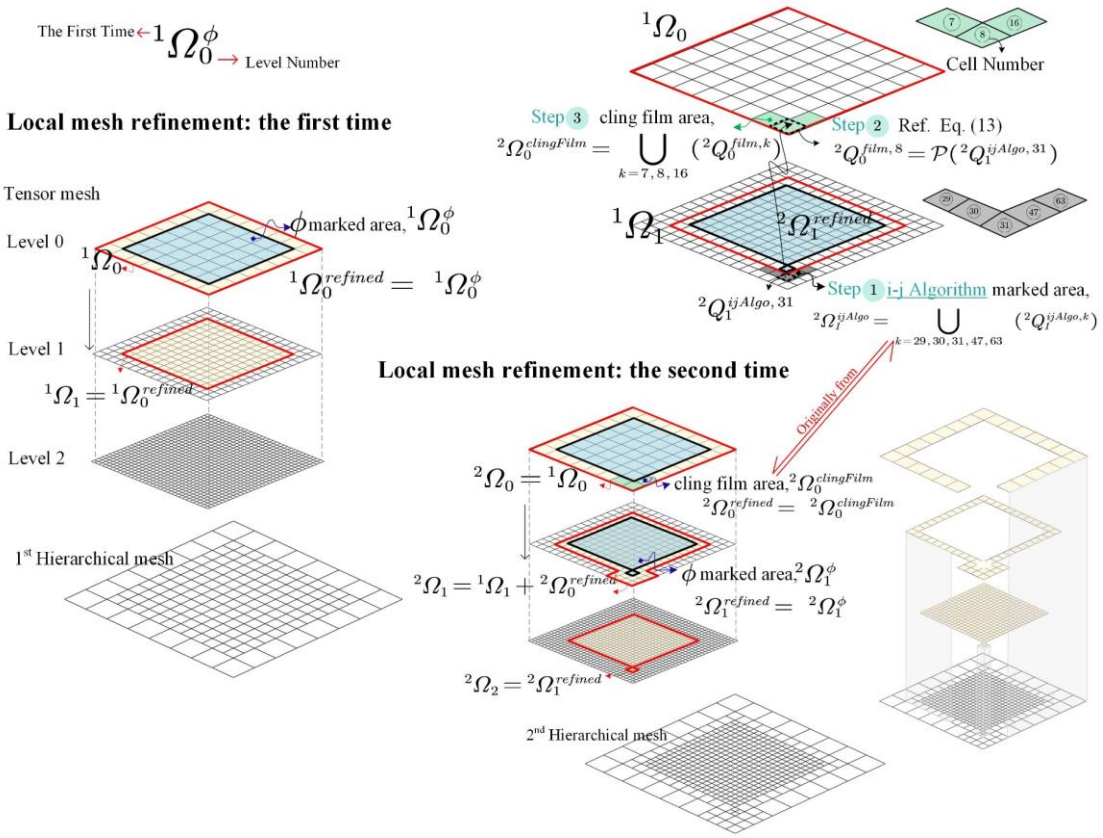

Fig. 5. A hierarchical mesh containing three levels for illustrating the cling film refinement criterion

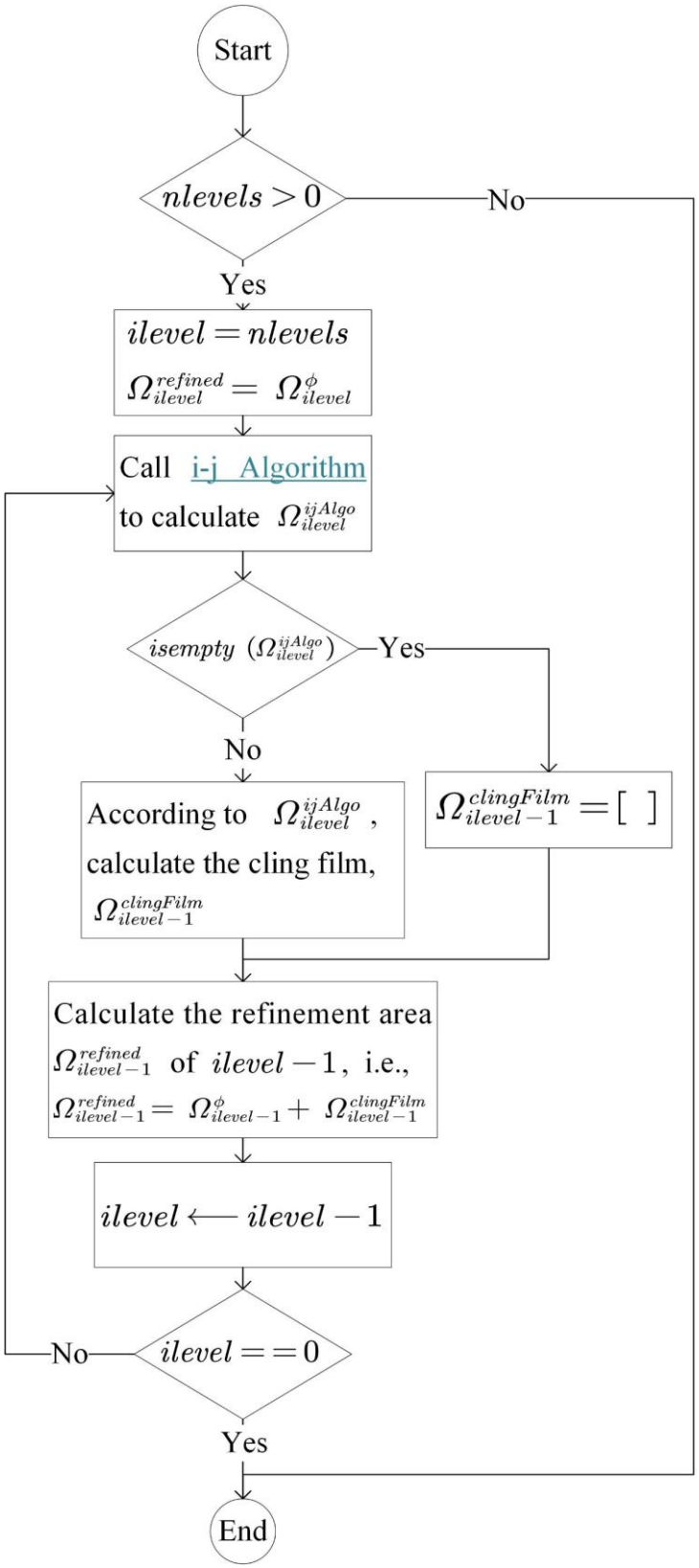

Fig. 6. Flow chart of the cling film method

Based on this, this manuscript proposes a novel refinement criterion, termed the cling film criterion. As seen in Figs. 5 and 6, the cling film criterion consists of two parts. The first part still utilizes the damage variable ϕ to mark the crack path region Ω_{ilevel}^{ϕ}. And the second part is to mark the refinement region $\Omega_{ilevel-1}^{clingFilm}$ with the aid of the proposed *i-j algorithm* (please see the source code in Appendix A) for guaranteeing the hierarchical difference of adjacent cells, and the entire process can be summarized as follows: (1) the *i-j algorithm* is employed to determine the marked region Ω_{ilevel}^{ijAlgo} of level $ilevel$; (2) If the region Ω_{ilevel}^{ijAlgo} is empty, it goes to the next level, and conversely marks its parent cell as the region $\Omega_{ilevel-1}^{clingFilm}$ to be refined in level $ilevel-1$. As depicted in the gray area ${}^{2}\Omega_{1}^{ijAlgo}$ and aqua green area ${}^{2}\Omega_{1}^{refined}$ in the upper right corner of Fig. 5, the cling film method only requires dealing with the cells in gray area, i.e., $\{Q|Q\in\mathcal{Q}_l\wedge Q\subset {}^{2}\Omega_{1}^{ijAlgo}\}$, thus reducing a certain number of computational cells compared to $\{Q|Q\in\mathcal{Q}_l\wedge Q\subset {}^{2}\Omega_{1}^{refined}\}$ (aqua green area) of the traditional method, especially in the fine mesh of the phase-field model. Besides, the effectiveness of the proposed criterion is also directly demonstrated by the hierarchical meshes in Fig. 5 in comparison with Fig. 7. Notably, whether in 2D or 3D, the proposed criterion only requires a simple addition or subtraction operation on the 1D knot vector of the IGA for determining Ω_{ilevel}^{ijAlgo} (as demonstrated in Appendix A), thus further reducing the computing cost to a certain extent.

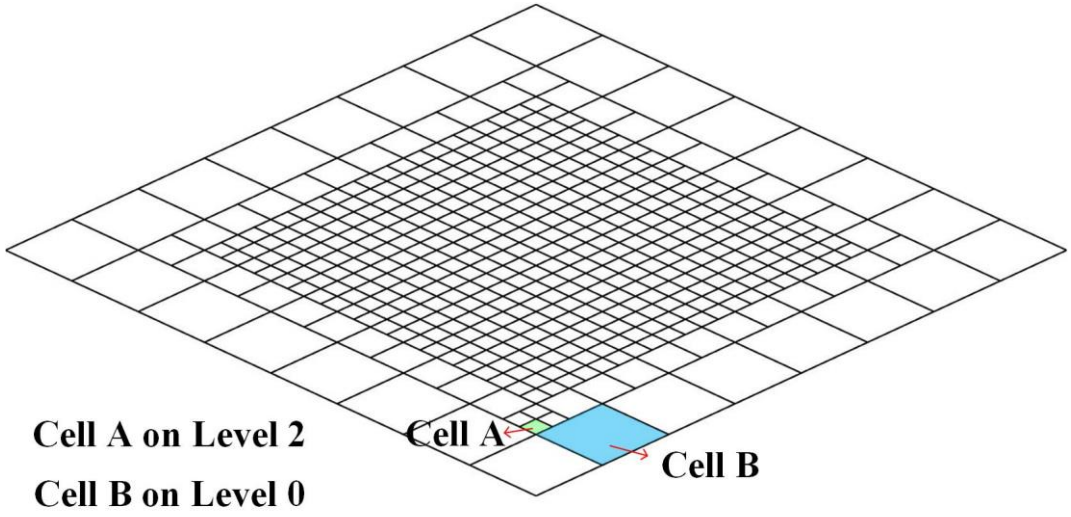

Fig. 7. Hierarchical meshes obtained by using damage variable ϕ as the refinement criterion

3.3.2 An improved data transfer operator

In adaptive analysis, the data transfer between meshes can be roughly divided into two categories: one for field variables located at nodes (or control points in IGA), e.g., damage variables ϕ or node displacements $\boldsymbol{u}$, and the other for history variables located at integration points, e.g., $H(\boldsymbol{x},t)$ in phase field models and plastic strains $\boldsymbol{\varepsilon}_p$ in inelastic materials.

For the first category, the authors utilize the approach of (Garau and Vázquez, 2018), i.e., Eq. (37) below, to transfer node variables.

$$^{k+1}\boldsymbol{u} = \boldsymbol{K}\,{}^{k}\boldsymbol{u} \tag{2}$$

where the elements in K can be found in (Garau and Vázquez, 2018). Notably, due to the structured and nested nature of the hierarchical splines, this data transfer process is error-free.

And for the second category, such as $H(\boldsymbol{x},t)$, the common used data transfer operators are, but not limited to, Closest Point Transfer (CPT) and Basis Function Transfer (BFT). For the CPT method, the history variable at the new integration point is directly taken from the nearest old integration point, which makes it efficient and simple to implement. However, this is also the main reason for its poor transfer accuracy. And for the BFT method, as its name suggests, the data transfer between meshes is achieved with the aid of nodes and basis functions on the old and new meshes, and the implementation of its global version can be summarized in the following three steps:

(a) In the old mesh ${}^{k}\mathcal{Q}$: project the history variables at the old integration points onto the old nodes (or control points in the IGA) using the basis function ${}^{k}\widetilde{\mathcal{H}}$. If the least square fitting method is employed, this process can be expressed as

$$\boldsymbol{M}\boldsymbol{\phi}^{Node} = \boldsymbol{f}^{intPoint} \tag{38}$$

where $\boldsymbol{M}$ and $\boldsymbol{f}$ can be expressed as follows, respectively

$$\boldsymbol{M}_{i,j} = \int_{\Omega} {}^{k}\tilde{\beta}_i \; {}^{k}\tilde{\beta}_j d\Omega \tag{39}$$

$$\left(\boldsymbol{f}^{intPoint}\right)_i = \int_{\Omega} {}^{k}\tilde{\beta}_i \, \phi^{intPoint} d\Omega \tag{40}$$

where the basis functions ${}^{k}\tilde{\beta}_i \in {}^{k}\widetilde{\mathcal{H}}$.

(b) From the old mesh ${}^{k}\mathcal{Q}$ to the new mesh ${}^{k+1}\mathcal{Q}$: project the history variables at the old nodes obtained from (a) to the new nodes, e.g., utilizing Eq.(2).

(c) In the new mesh ${}^{k+1}\mathcal{Q}$: interpolation is performed using the new node variables obtained from (b) and the basis functions ${}^{k+1}\tilde{\beta}_i \in {}^{k+1}\widetilde{\mathcal{H}}$ to get the history variables at the new integration points.

Although BFT obviously improves the transfer accuracy, its computational efficiency is lower than that of CPT and its implementation is complicated. Apart from that, the global version of BFT requires solving a large-scale linear system of equations, while its cell-by-cell version requires a full integration cell in order to provide a sufficient number of sample points for the least-square fitting (Hennig et al., 2018). In light of the above and inspired by the pioneering work of (Garau and Vázquez, 2018; Hennig et al., 2018), this manuscript makes certain improvements to the traditional BFT and terms the improved method as Hierarchical Basis Function Transfer, abbreviated as HBFT. As depicted in Figs. 8 and 9, a feature of HBFT is that the history variables $H(\boldsymbol{x},t)$ are transferred level by level, and the transfer steps between any adjacent levels are basically the same as those of the traditional BFT; another feature is that the basis functions and control points used in HBFT are derived from the tensor basis space $\mathcal{B}$ instead of the hierarchical basis space $\widetilde{\mathcal{H}}$. Based on this, the proposed HBFT can be regarded as an intermediate version. Therefore, it not only has the potential to avoid solving large-scale linear equations of the global version, but also alleviates, to a certian extent, the requirement of the cell-by-cell version for the full integration cell. Additionally, in order to reduce the computational cost and transfer errors (as depicted in Figs. 21 and 22), HBFT only transfers the history variables in the local region to be refined, while keeping those within the remaining regions unchanged, as also displayed in Fig. 8.

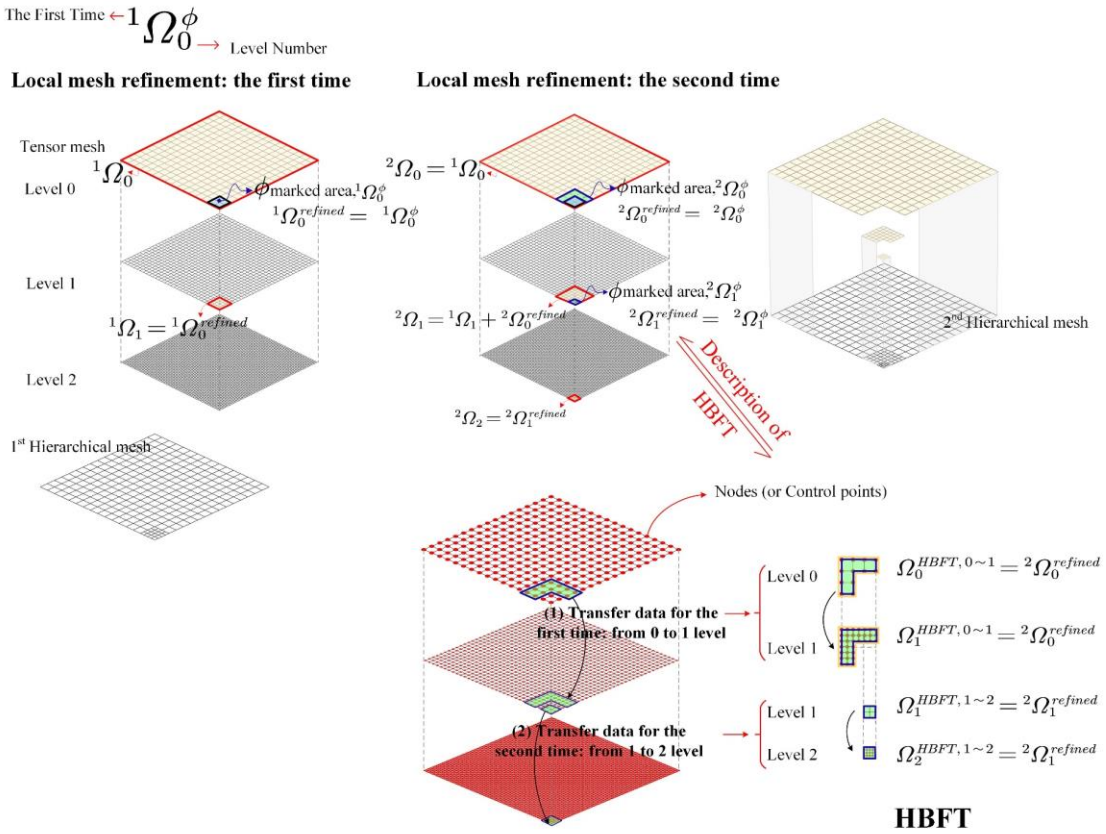

372

373 **Fig. 8.** A simple example to illustrate the proposed HBFT

374

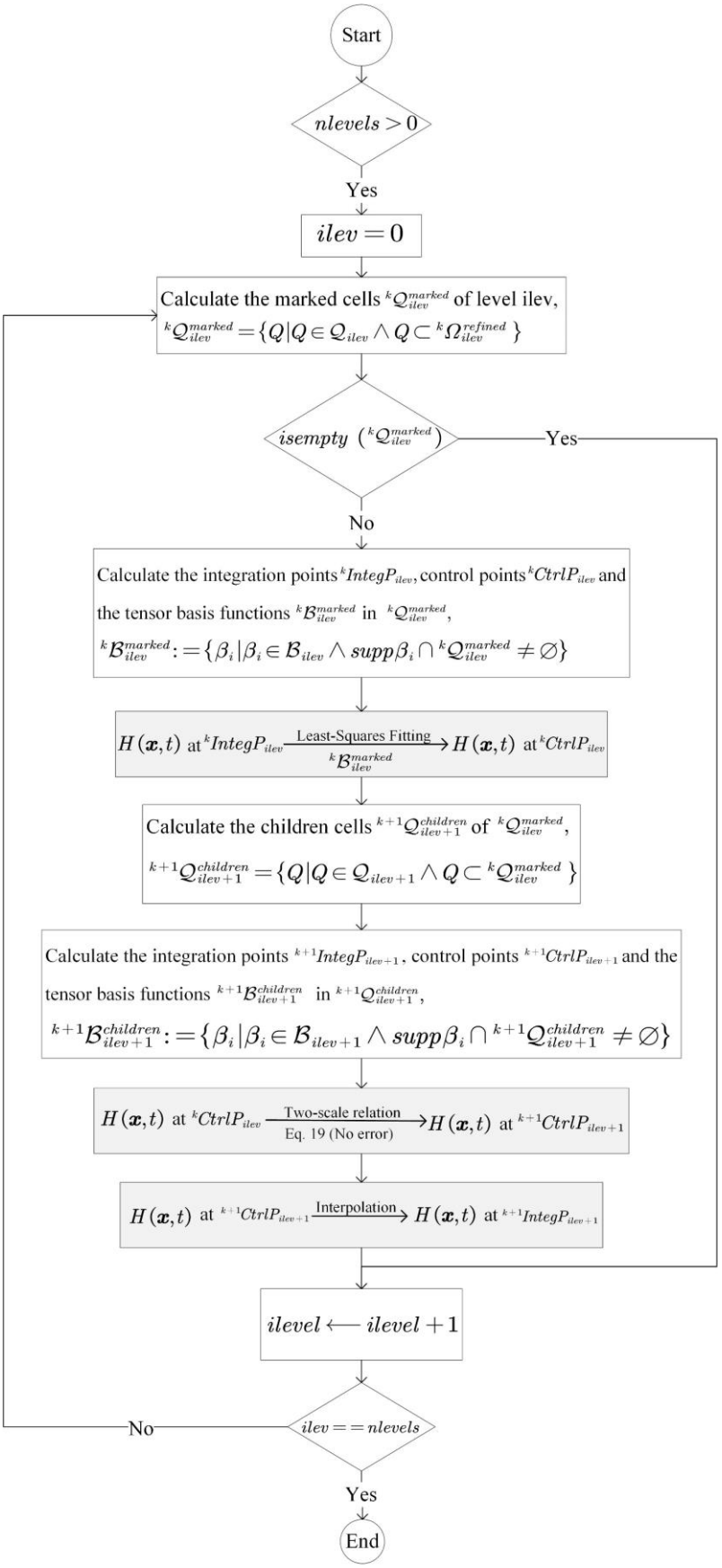

Fig. 9. Algorithm flow chart of the proposed HBFT

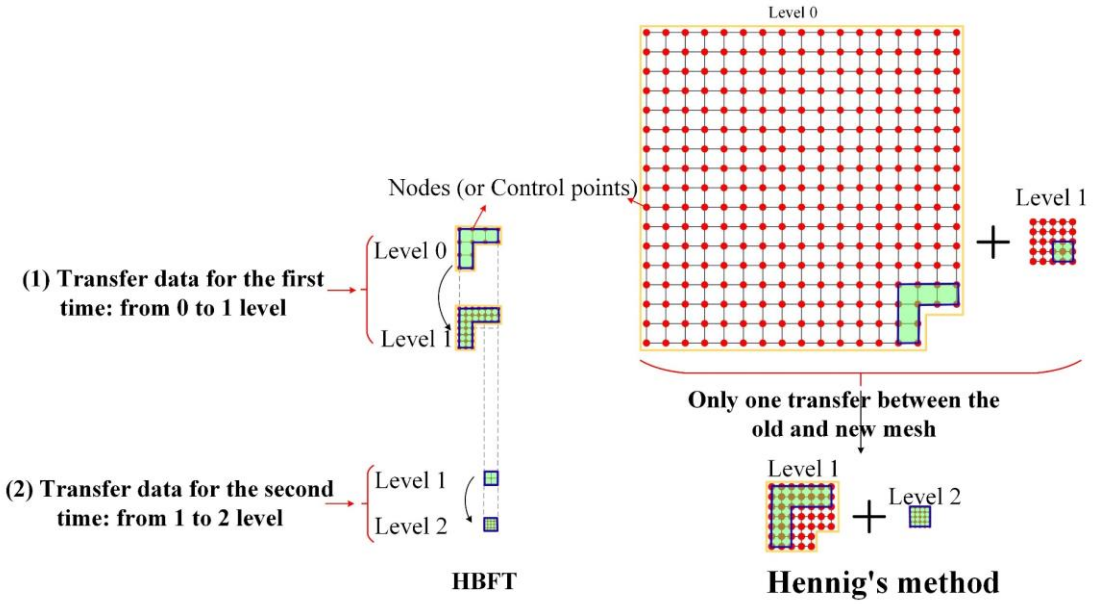

Fig. 10. A simple comparison of the proposed HBFT and Hennig's method

Finally, it is worth mentioning that the proposed HBFT reduces the number of basis functions and control points required in the intermediate steps compared to the method in (Hennig et al., 2018), as displayed in Fig. 10. In view of the above, the authors believe that the proposed HBFT is a simple and practical transfer operator.

4. Numerical examples

4.1 Single-edge notched pure shear example

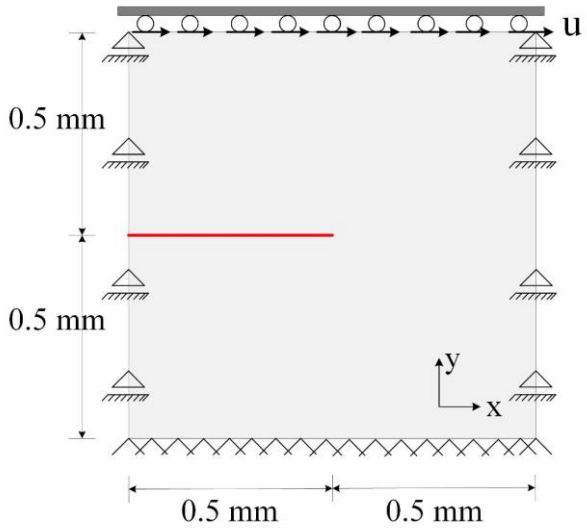

Fig. 11. Square specimen with a notch

The first example is a single-edge notched specimen in a pure shear loading mode. The specimen and constraints are depicted in Fig. 11. The length-scale parameter is $L_c = 0.0125$ mm, and other parameters are the same as in (Zhu et al., 2022). For this example, the cell size around the crack path is taken as $L_{h1} = 0.005\text{mm}$ (i.e., $L_c/L_{h1} = 2.5$), while the cell size far from the crack path is taken as $L_{h2} = 0.04\text{mm}$. This means that the side length of the coarse cell is 8 times longer than that of the fine cell (i.e., $L_{h2}/L_{h1} = 8$), and the area is 64 times larger. Additionally, to capture the crack paths accurately, the surrounding mesh of the initial preset crack is locally refined before the calculation, as shown in the first mesh discretization on the left in Fig.12.

As seen in Fig.12a and b, the crack paths obtained from the proposed mehtod and the uniform refinement are basically identical. The load-displacement curves in Fig. 13 also show the same results. It thus clear that the results of the proposed method are reliable. Besides, the spatial discretization (Fig. 12b) also indicates that the proposed refinement criterion is suitable for tracking crack nucleation and propagation in the fracture process. As described in Table 1, the calculation time of the proposed method is 97.17% lower than that of the uniform refinement, and the number of DOFs and cells are decreased by 91.42% and 90.69%, respectively. Additionally, Figs. 14 and 15 also further demonstrate the performance of the proposed method in terms of computing time and memory requirements.

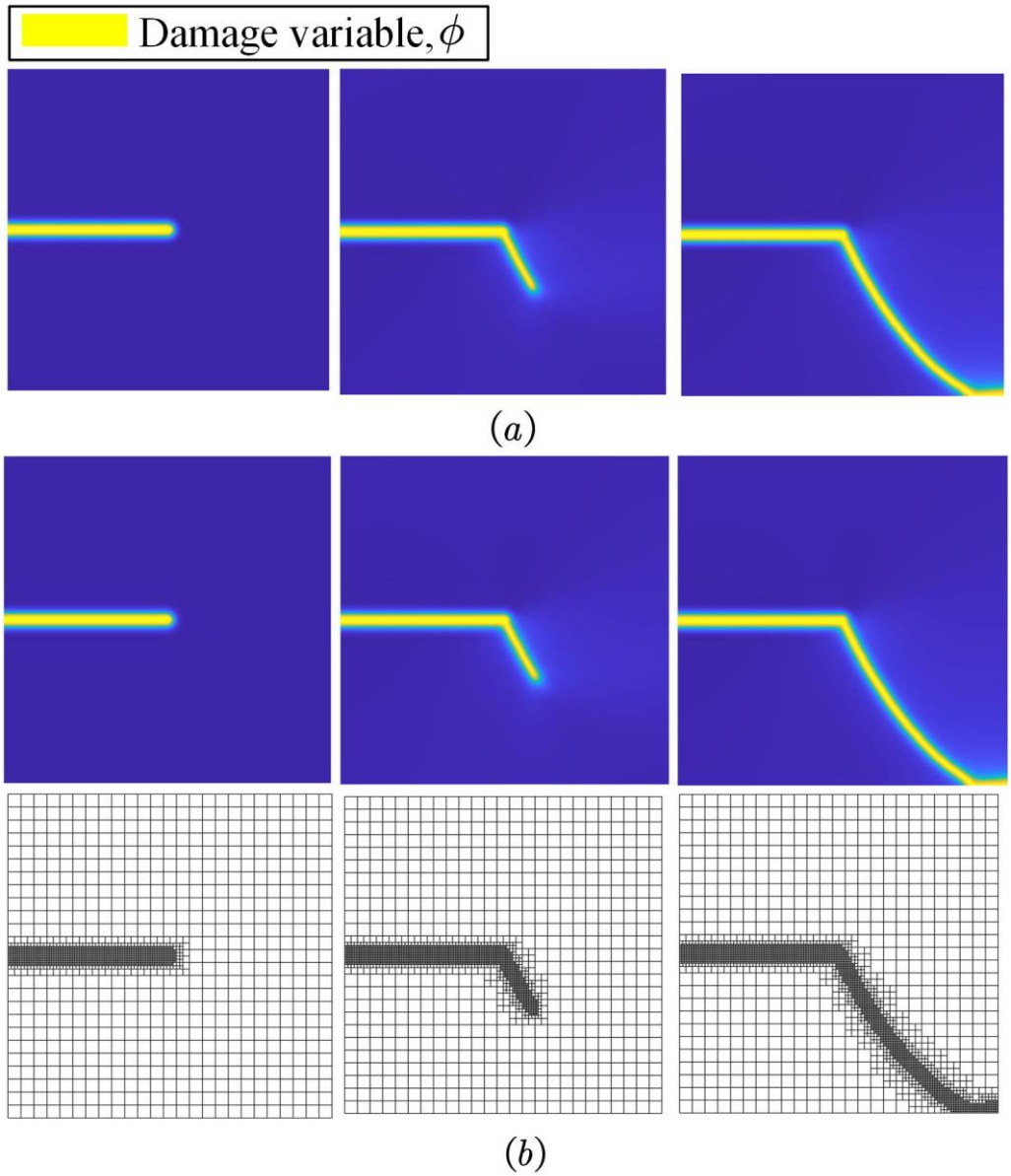

414

415 **Fig. 12.** Crack propagation and spatial discretizations for (a) the uniform refinement

416 and (b) the proposed method

417

418

419

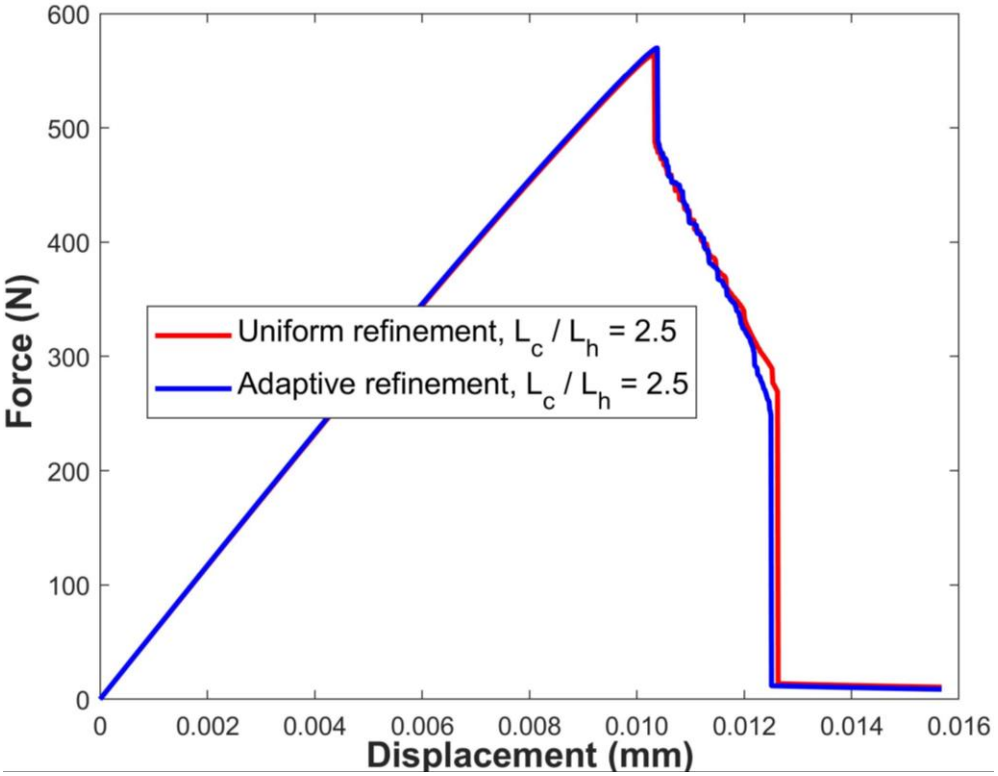

Fig. 13. Load-displacement curves obtained from the proposed method and the uniform refinement

Table 1

Computing time, number of DOFs and number of cells for the proposed method and the uniform refinement (single-edge notched sample)

Methods	Computing time (h)	Number of DOFs	Number of cells
The proposed method	0.2537	10506	3724
Uniform refinement	8.972	122412	40000

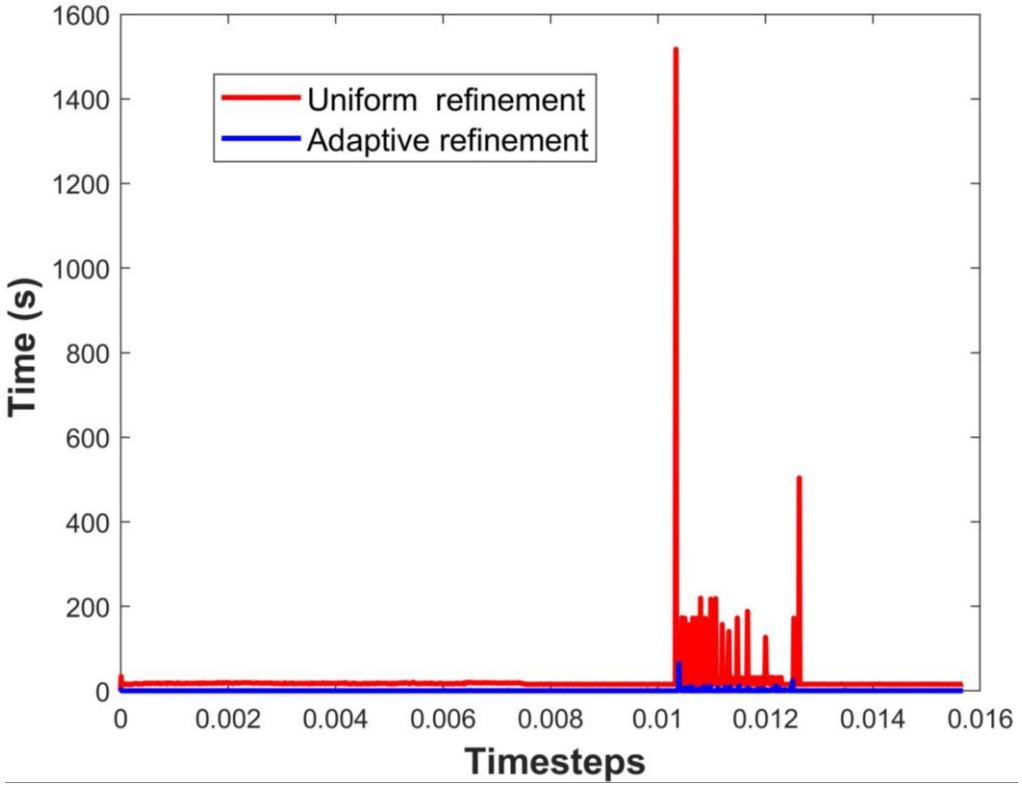

Fig. 14. Computing time at each time step

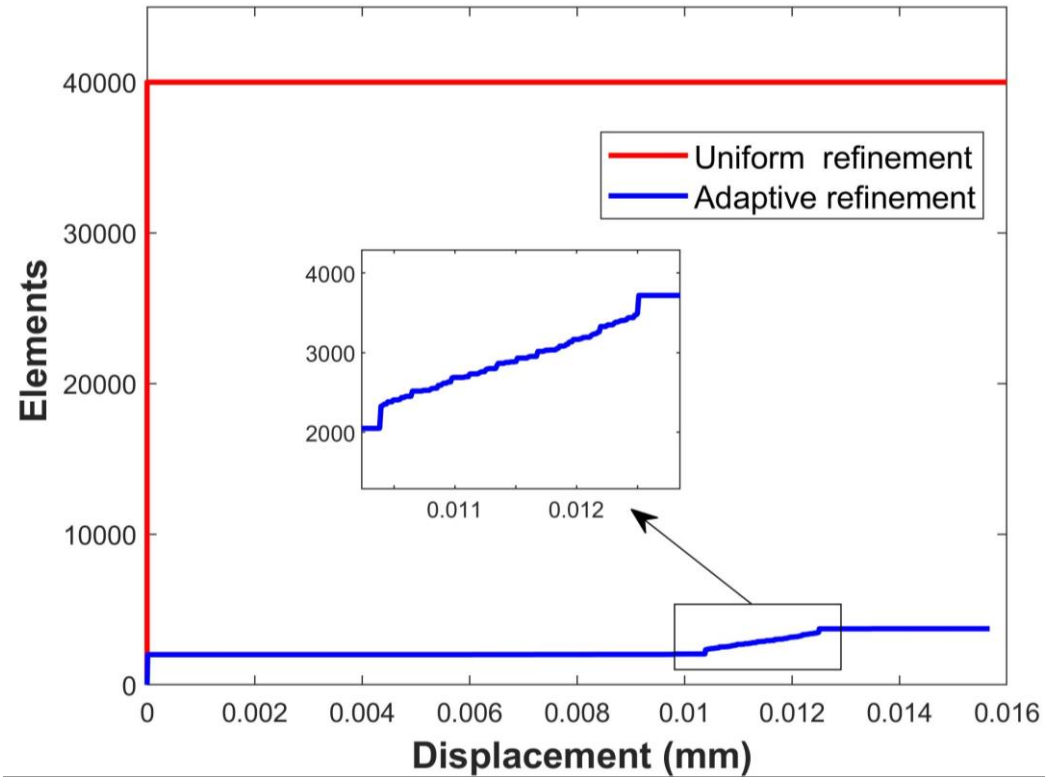

Fig. 15. Number of cells at each time step

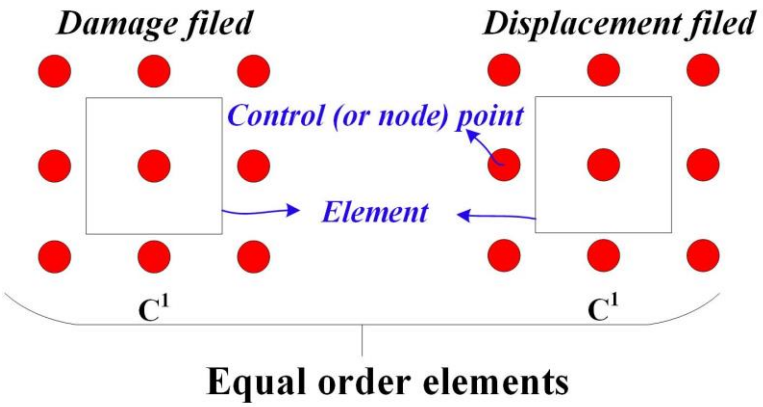

(a)

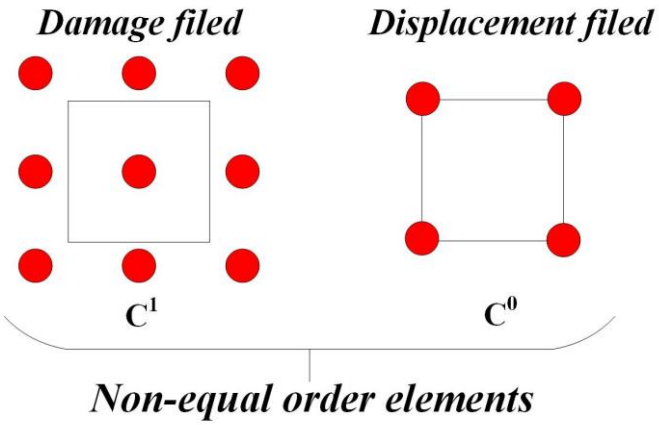

(b)

Fig. 16. Different cell combinations, (a) equal order cells and (b) non-equal order cells

Secondly, the authors study the influence of different cell combinations (as depicted in Fig 16) on computing efficiency and accuracy of the proposed method. Figs. 12b and 17 illustrate the final crack paths and spatial discretizations obtained using these two element combinations, whilst Fig. 18 depicts the load-displacement curves. It is shown that the simulations of the two cell combinations have the same accuracy. Table 2 then presents the calculation time and the number of cells. As detailed

in Table 2, the calculation time using non-equal order cells is 35.23% less than that of equal order cells. Therefore, if not explicitly stated, the non-equal order cells are used.

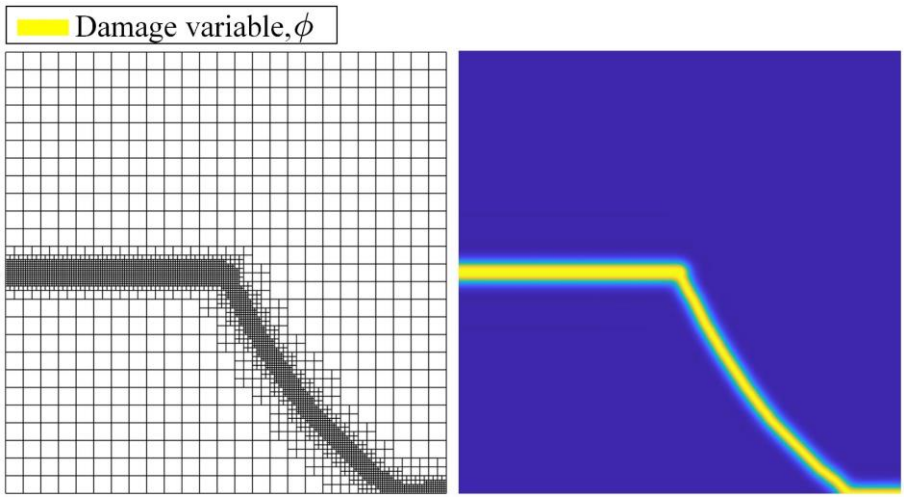

Fig. 17. Final crack paths and spatial discretizations obtained using the equal order cells

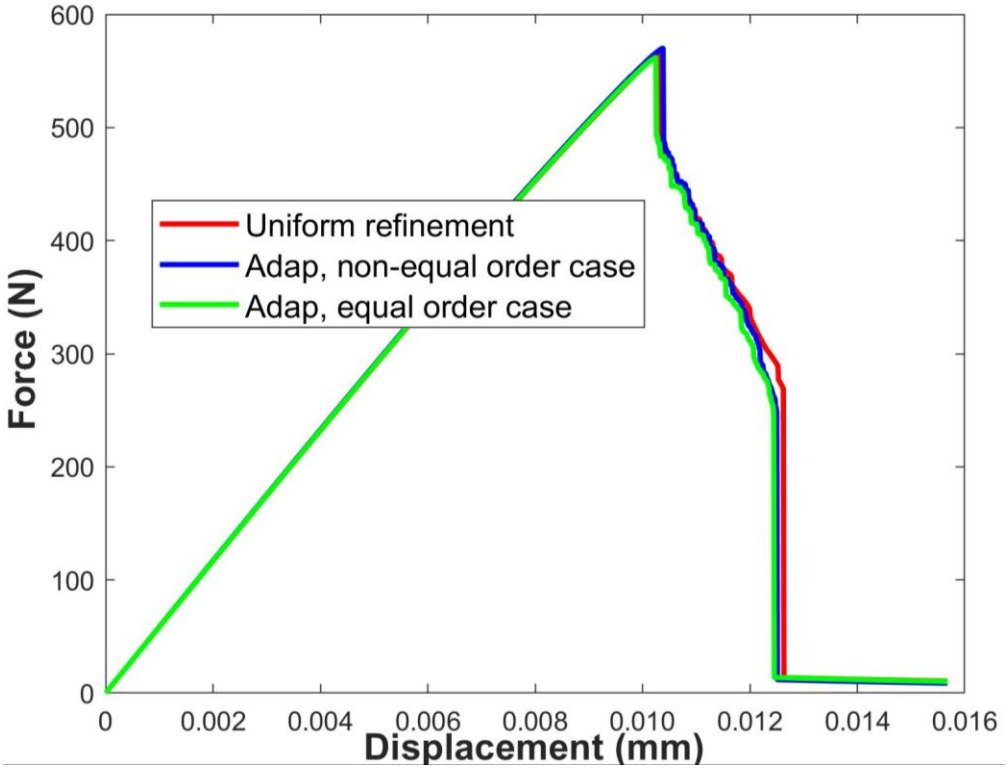

Fig. 18. Load-displacement curves obtained using the uniform refinement and the proposed method combining different cell combinations

Table 2

Computing time for the proposed method combining different cell combinations (single-edge notched sample)

cell combinations	Computing time (h)	Number of cells
Equal order cells	0.3917	3697
Non-equal order cells	0.2537	3724

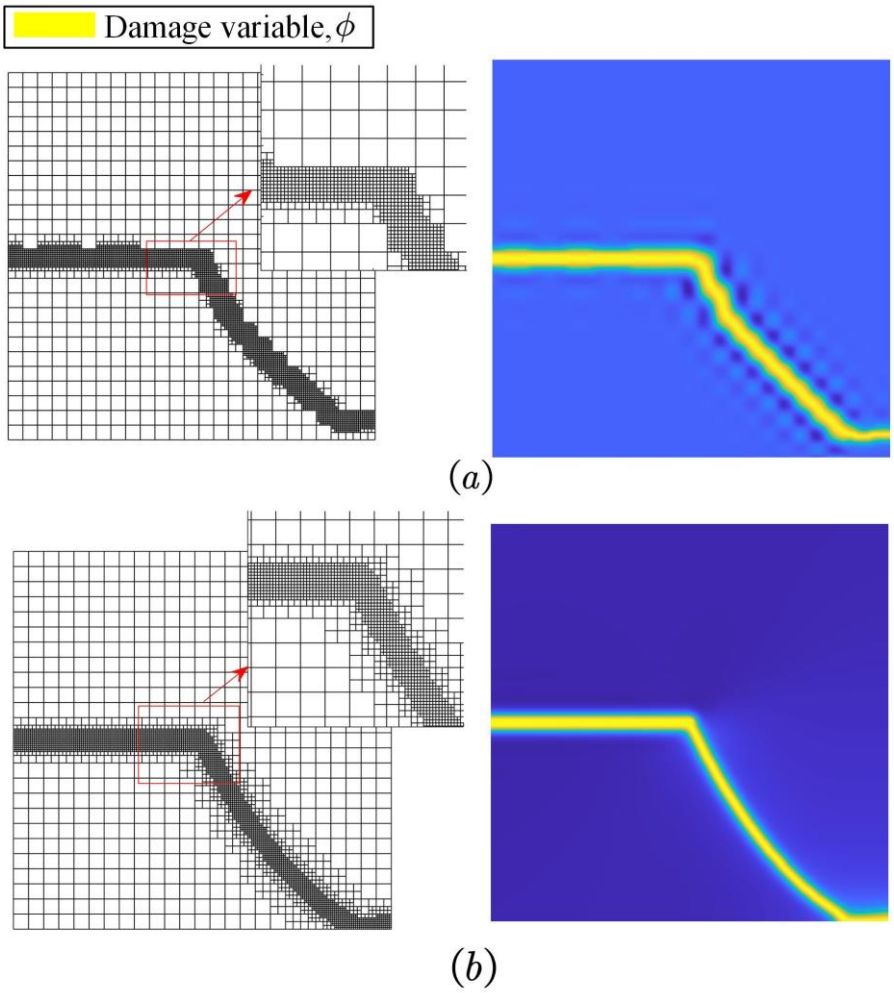

458

459 **Fig. 19.** Spatial discretizations obtained using (a) the damage variable ϕ and (b) the

460 proposed refinement criterion

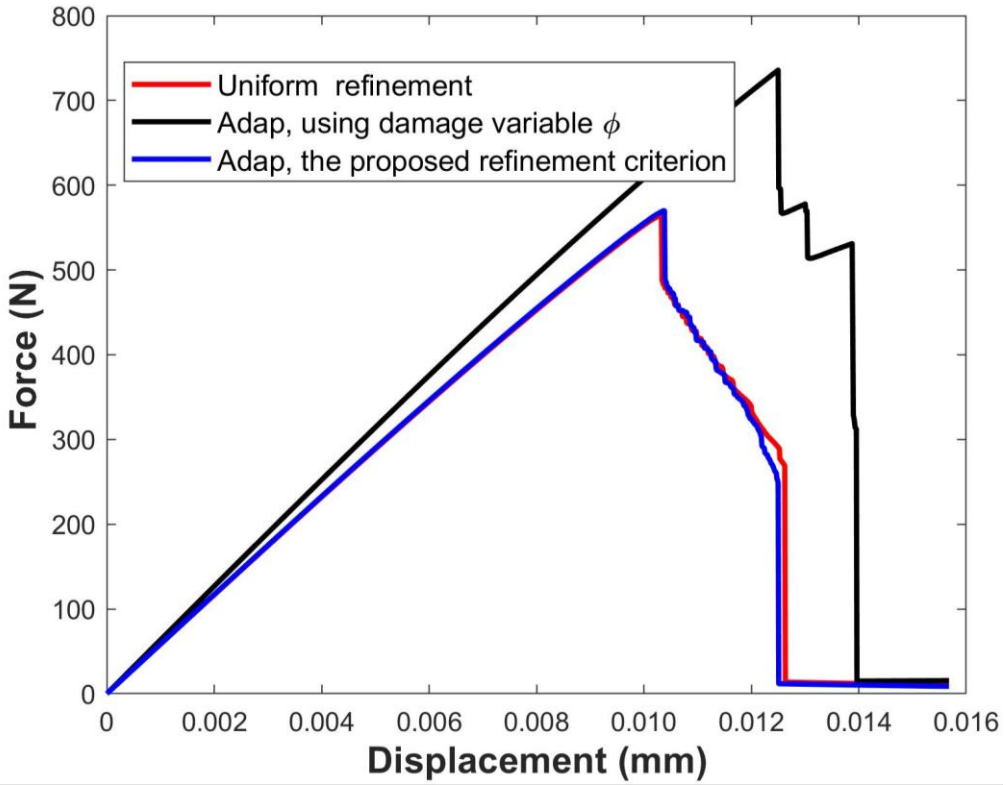

461

462 **Fig. 20.** Load-displacement curves obtained using the damage variable ϕ, the

463 proposed refinement criterion, and the uniform refinement, respectively

464

465 Thirdly, the authors briefly discussed the proposed refinement criterion and the

466 improved transfer operator, i.e., HBFT.

467 For the former, as depicted in Fig. 19a, when the damage variable ϕ is considered

468 as the refinement criterion, the maximum hierarchical difference between adjacent

469 elements is up to 3, and the corresponding crack path present obvious oscillations. In

470 contrast, the hierarchical difference of the proposed criterion is less than or equal to 1,

471 and the crack path (Fig. 19b) obtained therefrom is consistent with the uniform

472 refinement (Fig. 12a). The load-displacement curves in Fig 20 also show the same

473 trend. These simulations preliminarily demonstrate the performance of the proposed
474 criterion.

475 And for the latter, i.e., the proposed HBFT, will be briefly discussed here. Notably,
476 for most monotonic loading cases, the adaptive phase-field method can also adopt the
477 initial strain-history function $H(x,0)$ instead of the data transfer operator. Therefore,
478 this situation is also discussed here. As seen in Fig. 21, the final crack path obtained
479 from the proposed HBFT are essentially the same as those from the uniform refinement
480 and $H(x,0)$, while the crack path obtained from the global version of the traditonal
481 transfer operator have certain deviations. This is also indicated by the spatial
482 discretizations displayed in Fig. 21. Besides, the Load-displacement curves (as shown
483 in Fig. 22) obtained using various data transfer operators also show the same trend, and
484 the results of the proposed HBFT are closest to that of the uniform refinement. As for
485 efficiency, the computational time of the proposed HBFT is reduced by 20.41%
486 compared to $H(x,0)$, while it is 94.38% less than the global version of the traditional
487 transfer operator. In light of the above and Figs. 8 and 9, the authors believe that the
488 proposed HBFT is a simple and practical operator with certain advantages in terms of
489 computational efficiency and accuracy. Finally, it should be noted that only a
490 preliminary validation of the proposed HBFT has been performed in this paper. And its
491 performance in non-monotonic loading and other complex cases will be analyzed in
492 authors' future work.

493

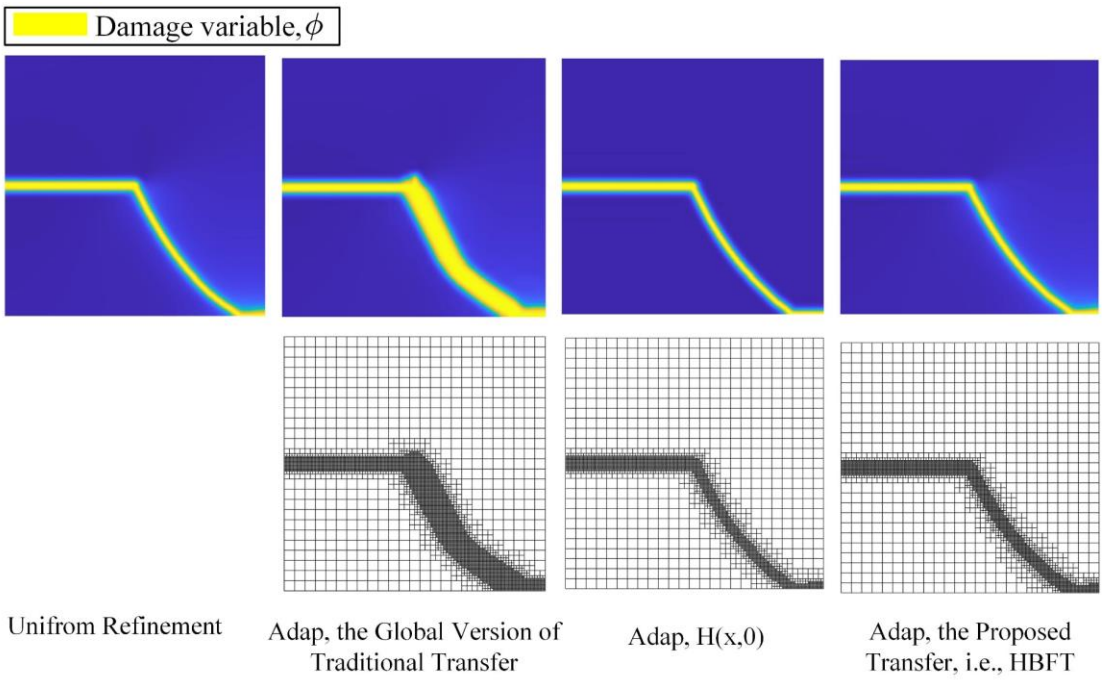

Fig. 21. Final crack paths and spatial discretizations obtained using the uniform refinement, the global version of traditional transfer, the initial strain-history function $H(x,0)$ and the proposed transfer operator, i.e., HBFT.

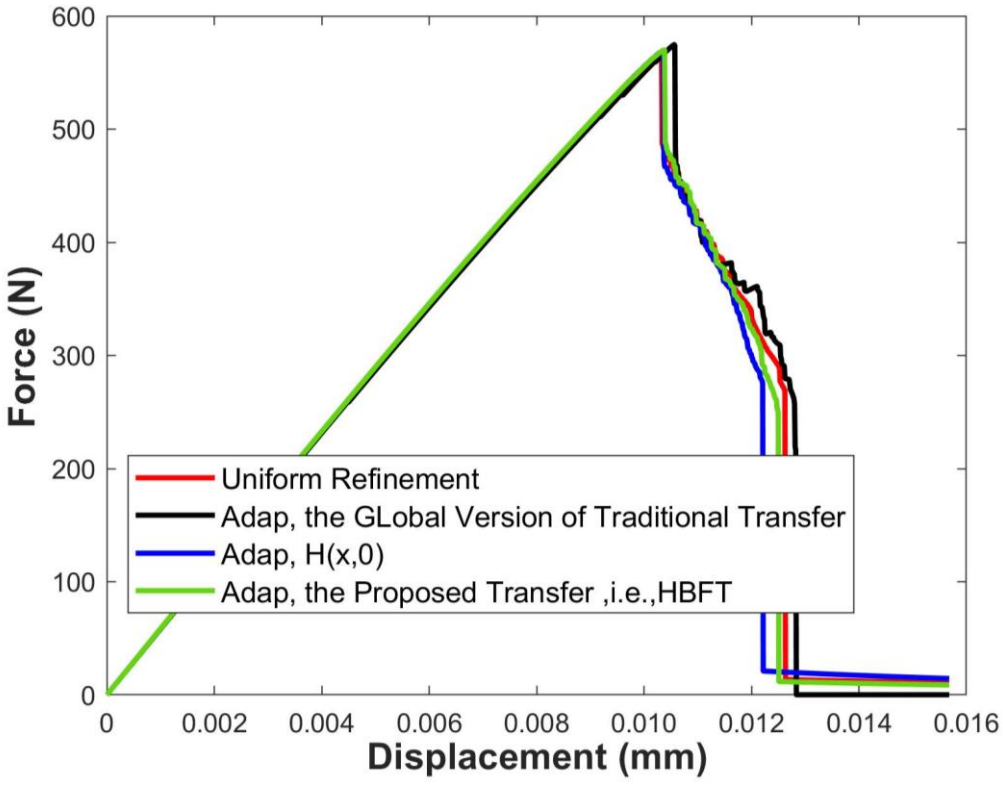

Fig. 22. Load-displacement curves obtained using the uniform refinement, the global version of traditional transfer, the initial strain-history function $H(x,0)$ and the proposed transfer operator, i.e., HBFT.

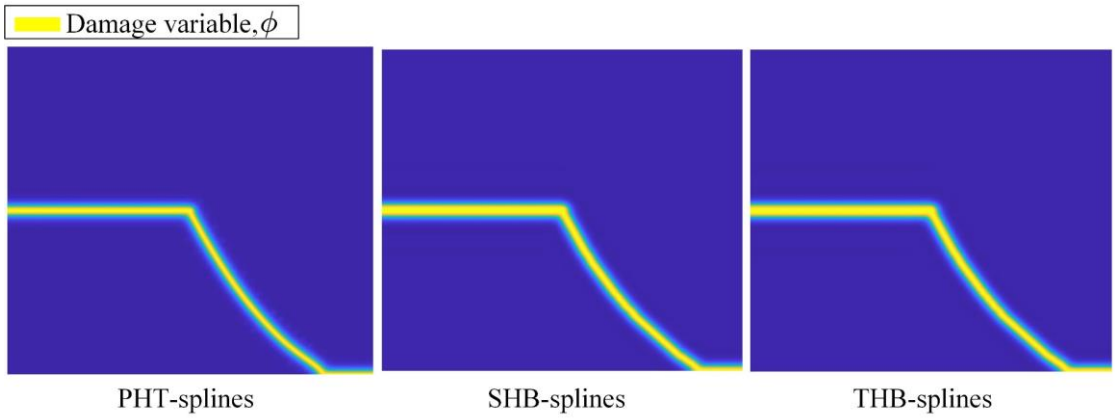

Fig. 23. Crack paths obtained from these three adaptive phase-field methods

Finally, the authors present a brief comparison of adaptive phase-field methods based on three different kinds of splines (i.e., SHB-splines, THB-splines, and PHT-splines). The crack paths obtained from SHB-splines, THB-splines, and PHT-splines (Goswami et al., 2020c), respectively, are given in Fig. 23, and the corresponding force-displacement curves are depicted in Fig. 24. As depicted, the calculation accuracy of these three methods is basically the same. For the slight difference in the peak points, the authors believe that it may be due to the different refinement criteria (or error estimators) used in this manuscript and (Goswami et al., 2020b). Additionally,

(1) the computation time of SHB-splines (0.2383h) is basically the same as that of THB-splines (0.2096h);

(2) The number of non-zero elements in the stiffness matrix of SHB-splines is 28% more than that of THB-splines. However, THB-splines requires real-time modifications of the basis functions (i.e., so-called truncation) during the adaptive process, which can cause some difficulties in assembling the stiffness matrix and transferring variables between the old and new meshes;

(3) the computation time of PHT-splines (0.6952h) is higher than that of SHB-splines and THB-splines. It should be noted that (Goswami et al., 2020b)'s work is outstanding and meaningful. The authors have only made a cursory comparison in a simple situation.

Taking into account the computation time and the difficulty of numerical implementation, the authors believe that the SHB-splines based adaptive phase-field method may be a suitable option. Overall, the authors provide a brief comparison of these three adaptive phase-field methods. It should be noted that there are many factors that have not yet been considered, which will be analyzed in detail in the authors' future work.

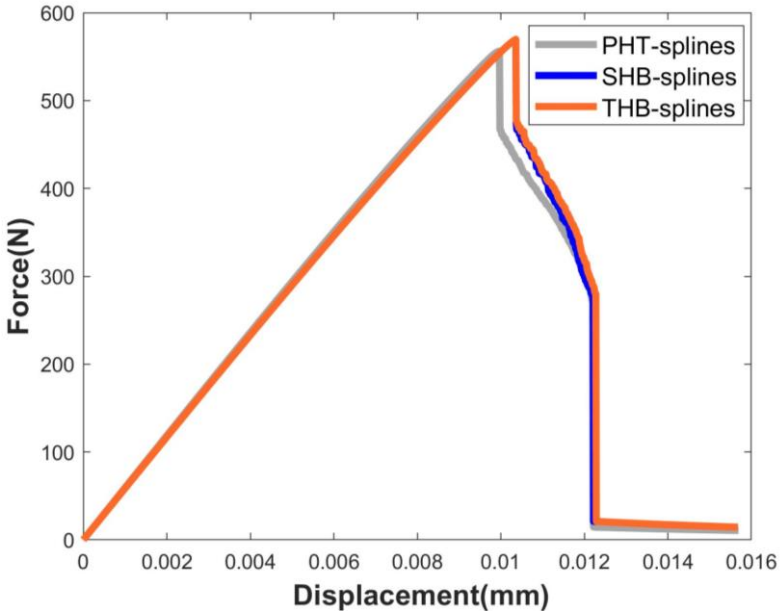

Fig. 24. Force-displacement curves obtained from these three adaptive phase-field methods

4.2 Rock-like specimen including multiple fractures

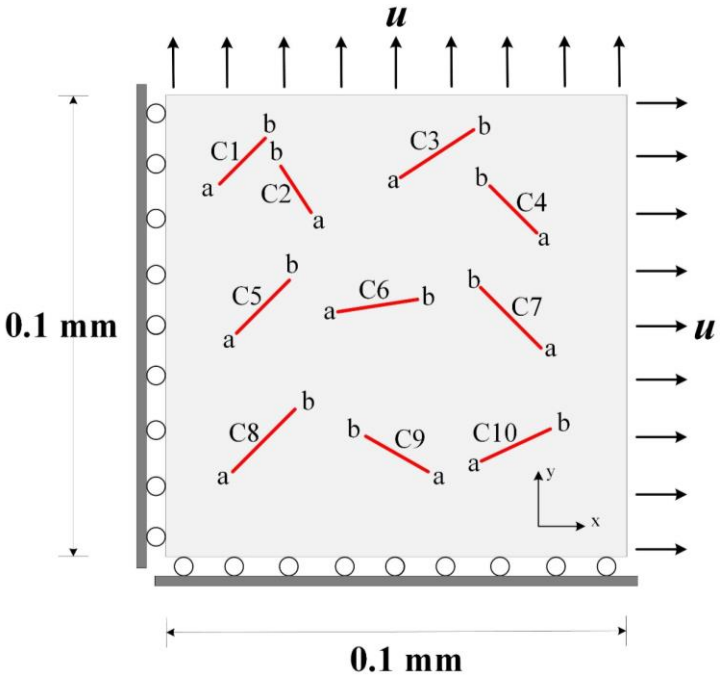

Fig. 25. Rock-like specimen including multiple fractures

537

538 The second example simulates multi-crack extension and coalescence in
539 geotechnical engineering. The specimen and constraints are illustrated in Fig. 25. The
540 length-scale parameter is $L_c = 1 \times 10^{-3}$ mm, the cell size is $L_c/L_h = 2$, and other
541 parameters are the same as in (Zhu et al., 2022)

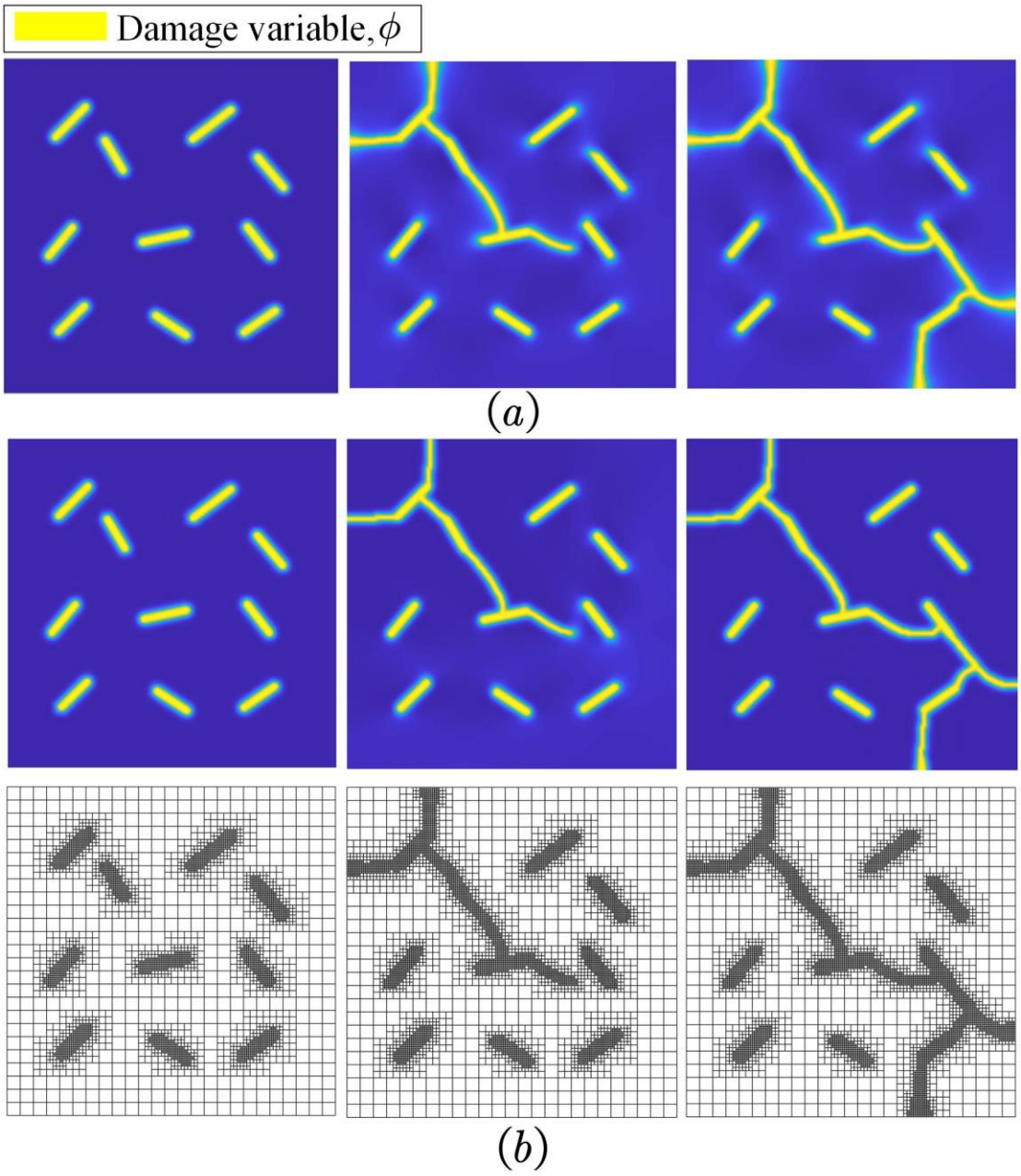

542

Fig. 26. Crack propagation and spatial discretizations for (a) the uniform refinement and (b) the proposed method

Fig. 26 presents the process of crack extension obtained using the proposed method and the uniform refinement, respectively, where an excellent concordance is obtained. The load-displacement curves in Fig. 27 also demonstrate the accuracy of the proposed method. Additionally, comparing the fracture paths and meshes in Fig. 26 b, it is clear that the proposed method is capable of local mesh adaption along the crack extension. Table 3 below provides the computing time, number of DOFs, and number of cells for the proposed method and the uniform refinement. As detailed in Table 3, the calculation time of the proposed method is 95.82% lower than that of the uniform refinement, and the number of DOFs and cells are decreased by 84.89% and 82.57%, respectively.

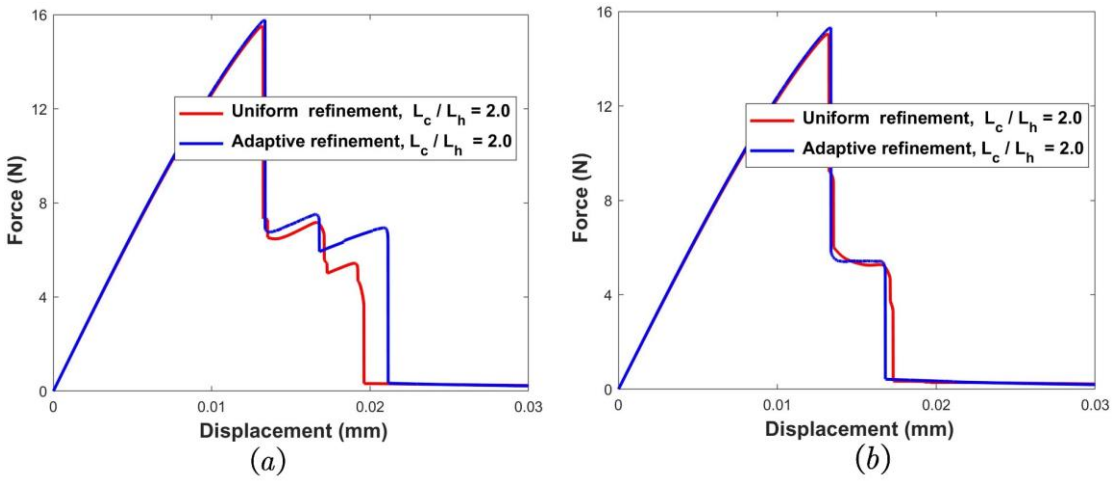

Fig. 27. Load-displacement curves at (a) the right edge and (b) the top edge, respectively

Table 3

Calculation time and storage requirements for the proposed method and the uniform refinement (Rock-like specimens including multiple fractures)

Methods	Computing time (h)	Number of DOFs	Number of cells
The proposed method	0.9282	18501	6970
Uniform refinement	22.1903	122412	40000

4.3 Brazilian disc test

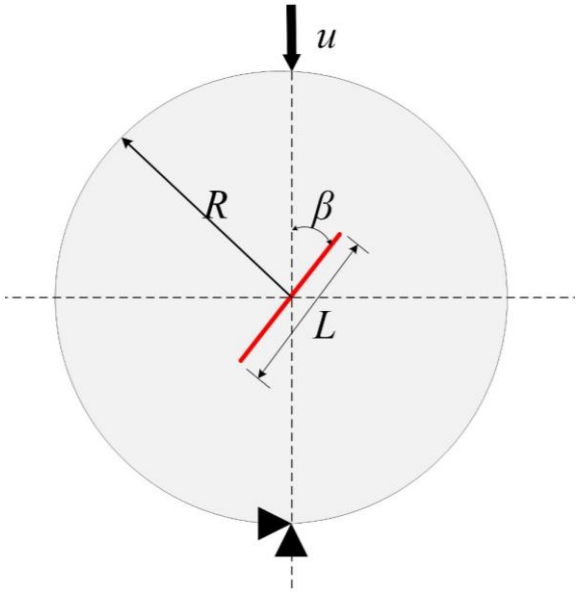

Fig. 28. Brazilian disc model

The third example is the Brazilian disc test (Zhou et al., 2020), which is principally used for measuring the tensile strength of rocks. The specimen and constraints are displayed in Fig. 28. Three fracture inclinations are considered, i.e., β = 30°, 60°, and 75° respectively. The length-scale parameter is $L_c = 2\text{mm}$, the cell size is $L_c/L_h = 2.0$, and the displacement increment is $\Delta u = 2 \times 10^{-5}\text{mm}$. Besides, other parameters are taken from (Zhou et al., 2020)

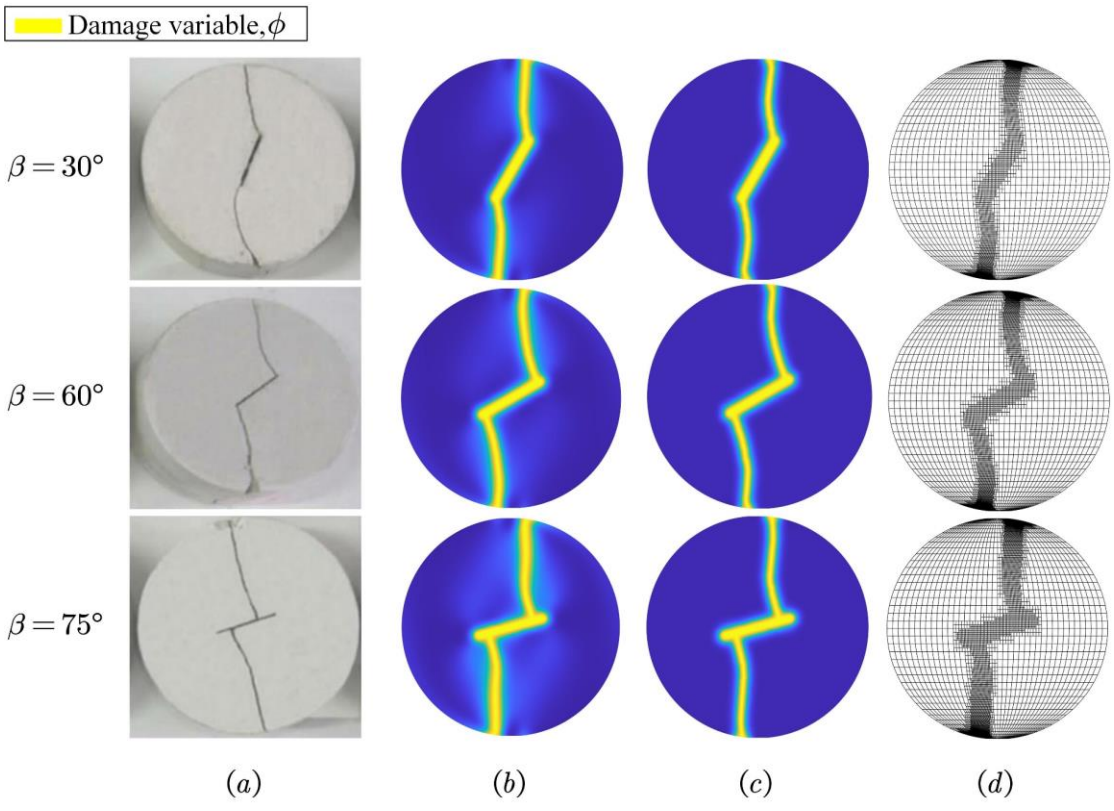

Fig. 29. Final crack paths and spatial discretizations resulting from (a) the experiment (Zhou et al., 2020), (b) the uniform refinement, (c) the proposed method, and (d) the proposed method, respectively, at different crack inclinations.

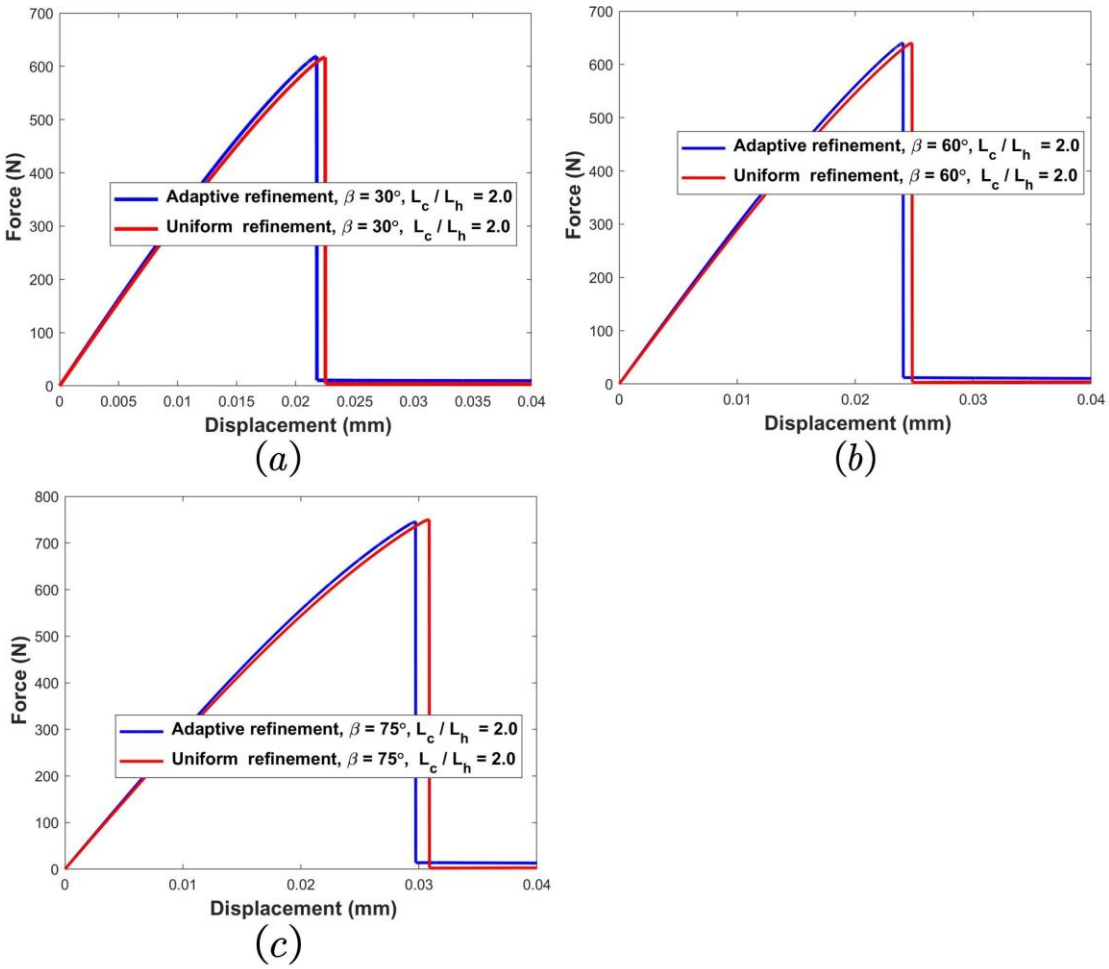

579

580 **Fig. 30.** Load-displacement curves obtained using the proposed method and the
581 uniform refinement, (a) $\beta = 30°$, (b) $\beta = 60°$, and (c) $\beta = 75°$.

582

583 Fig. 29 provides the crack propagation and spatial discretizations at three dipping
584 angles obtained from experiments (Zhou et al., 2020), the uniform refinement and the
585 proposed method. As seen, the fracture paths resulting from the proposed method are
586 basically the same as those from the other two methods. The load-displacement curves
587 depicted in Fig. 30a, b and c are also almost identical. It is thus clear that the proposed
588 method is reliable. Table 4 below provides the computing time, number of DOFs, and
589 number of cells obtained using the proposed method and the uniform refinement,

respectively. As shown in Table 4, the calculation time of the proposed method is 92.26%, 92% and 93.28% less than the uniform refinement in the three cases, respectively, while the number of DOFs and the number of cells are reduced by more than 75% overall.

Table 4

Computing time, number of DOFs and number of cells for the proposed method and the uniform refinement (Brazilian disc test)

Inclination angles	Methods	Computing time (h)	Number of DOFs	Number of cells
$\beta = 30°$	The proposed method	0.5731	16629	5608
	Uniform refinement	7.4003	75366	24336
$\beta = 60°$	The proposed method	0.6609	17307	5851
	Uniform refinement	8.2585	75366	24336
$\beta = 75°$	The proposed method	0.5516	18186	6178
	Uniform refinement	8.2141	75366	24336

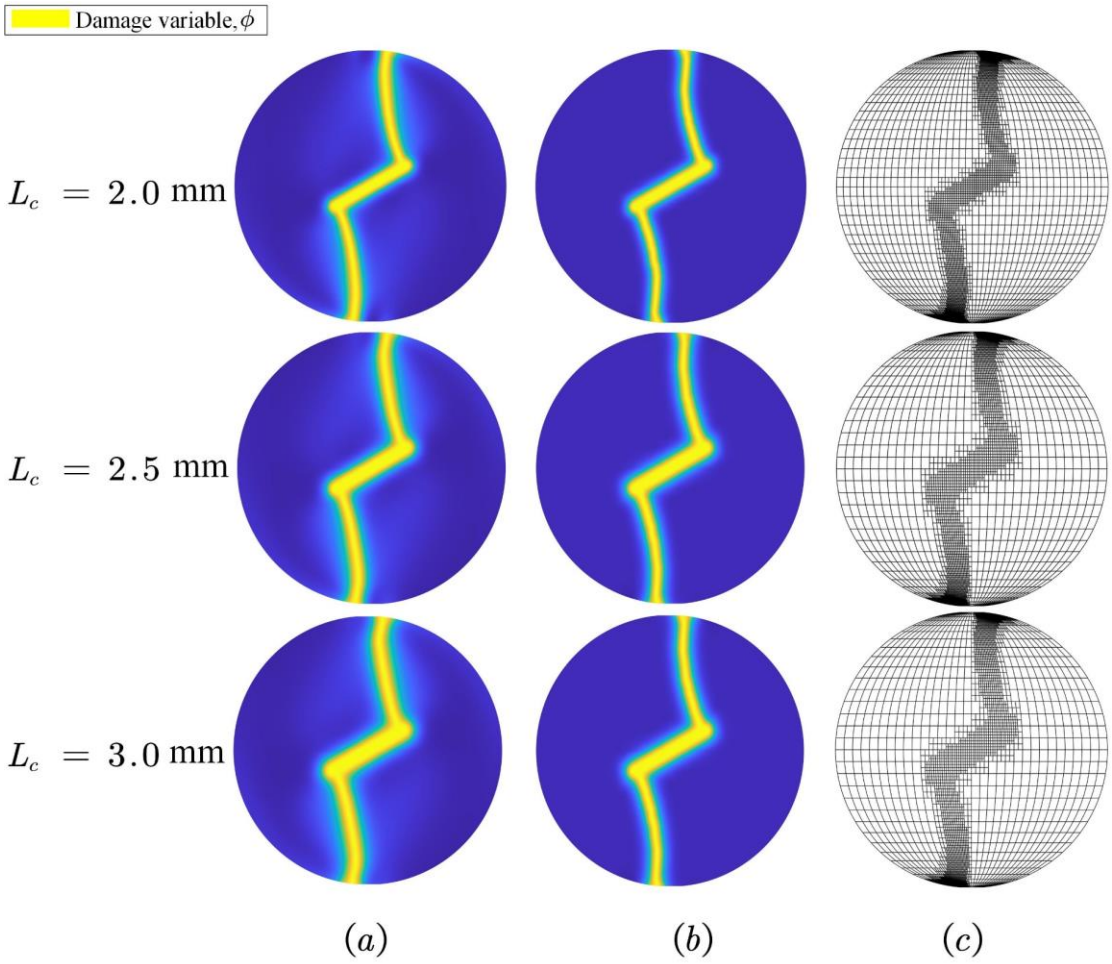

Fig. 31. Final crack paths and spatial discretizations obtained using (a) the uniform refinement, (b) the proposed approach, and (c) the proposed approach, respectively, for different length-scale parameters.

In addition, the authors also analyzed the influence of the length-scale parameter (for fixed L_c/L_h ratio) on the proposed approach. Take the Brazilian disc with $\beta = 60^o$ as an example. The length-scale parameters are chosen as 2.0 mm, 2.5 mm and 3.0 mm respectively, while the ratio of length-scale parameters to element sizes is held at 2.0. Fig. 31 presents the final crack paths and spatial discretizations resulting from the proposed approach and the uniform refinement for different length-scale parameters,

610 while Fig. 32 displays the corresponding force-displacement curves. As illustrated, the

611 width of the crack path broadens progressively with increasing L_c, whereas the peak

612 of the force-displacement curve varies in the opposite direction.

613

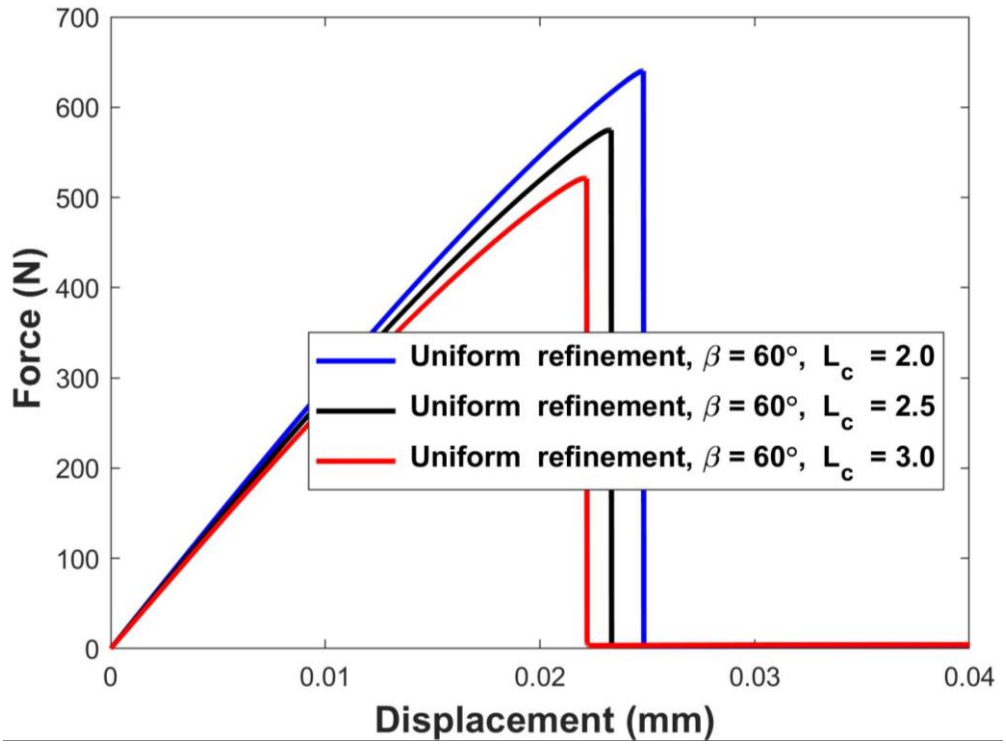

614

615 (a)

616

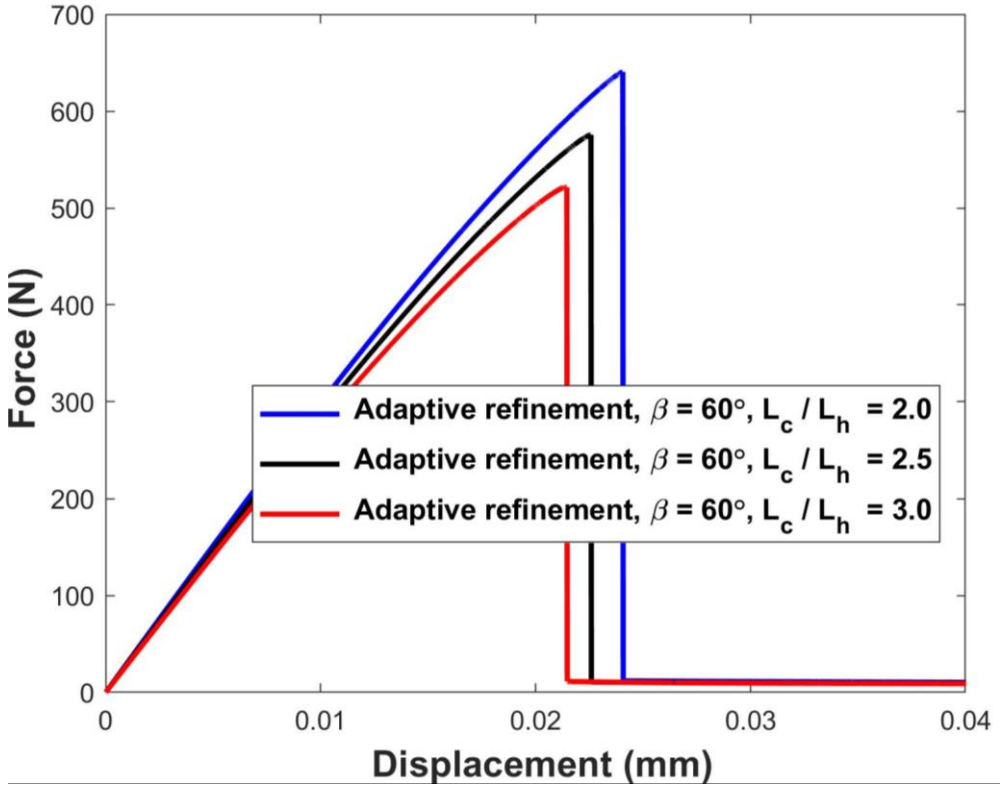

(b)

Fig. 32**.** Force-displacement curves for different length-scale parameters obtained from (a) the uniform refinement and (b) the proposed approach, respectively

4.4 Rock model including multiple fractures

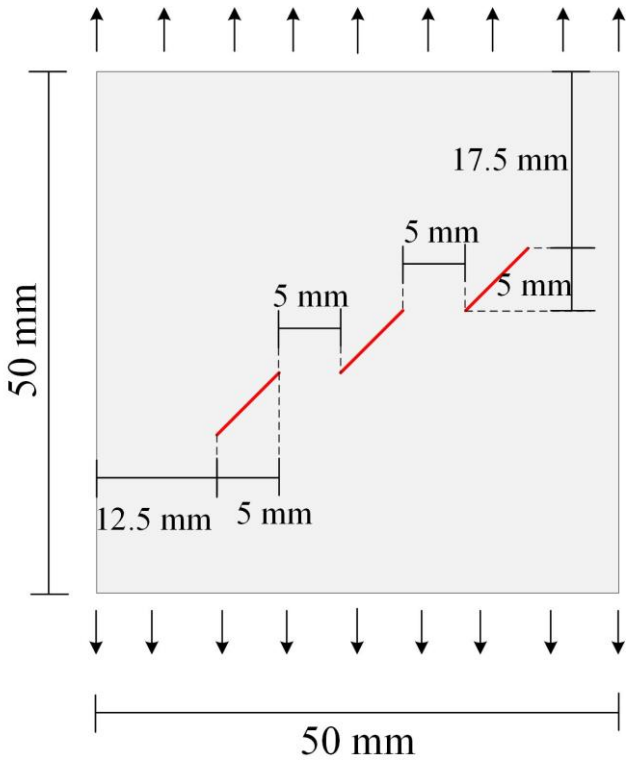

Fig. 33. Rock model including multiple fractures

This example also simulates the multi-crack extension issue in geotechnical engineering. The specimen and constraints are depicted in Fig. 33. The length-scale parameter is $L_c = 0.75\text{mm}$, the cell size is $L_c/L_h = 3.0$, and the displacement increment is $\triangle u = 6 \times 10^{-6}\text{mm}$. In additon, other material parameters are taken from (Zhou et al., 2018b).

As shown in Figs. 34 and 35, the mesh discretization of the proposed method is capable of continuous local refinement with crack extension, and the resulting crack paths and load-displacement curves are also consistent with the results of uniform refinement. This indicates that the proposed method has the ability to simulate multi-

crack extension in geotechnical engineering. For computational efficiency (Table 5), the calculation time, number of DOFs and number of cells obtained from the proposed method are 97.84%, 92.03% and 91.29% lower than those of the uniform refinement, respectively.

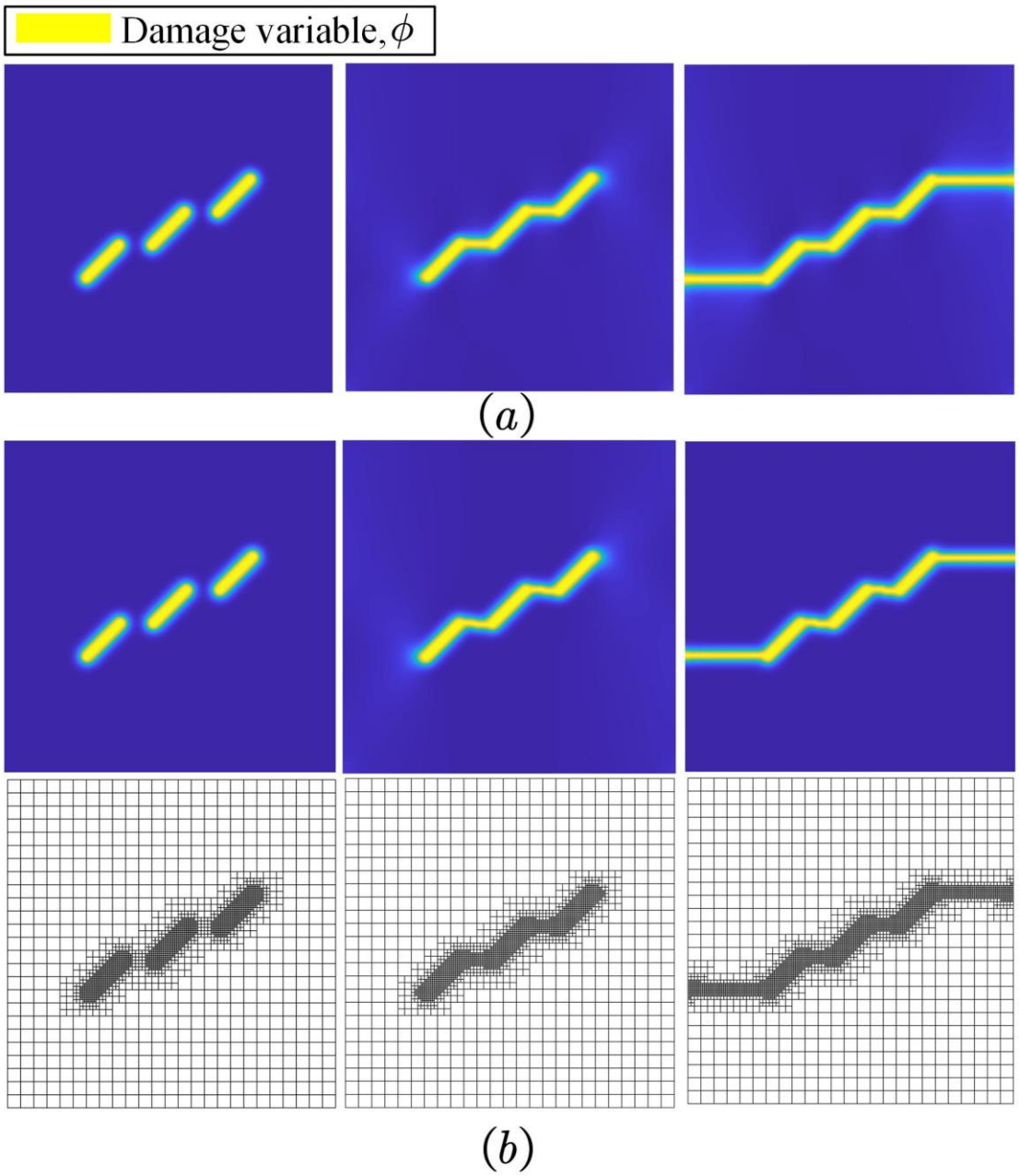

Fig. 34. Final crack paths and spatial discretizations resulting from (a) the uniform refinement, (b) the proposed method, respectively

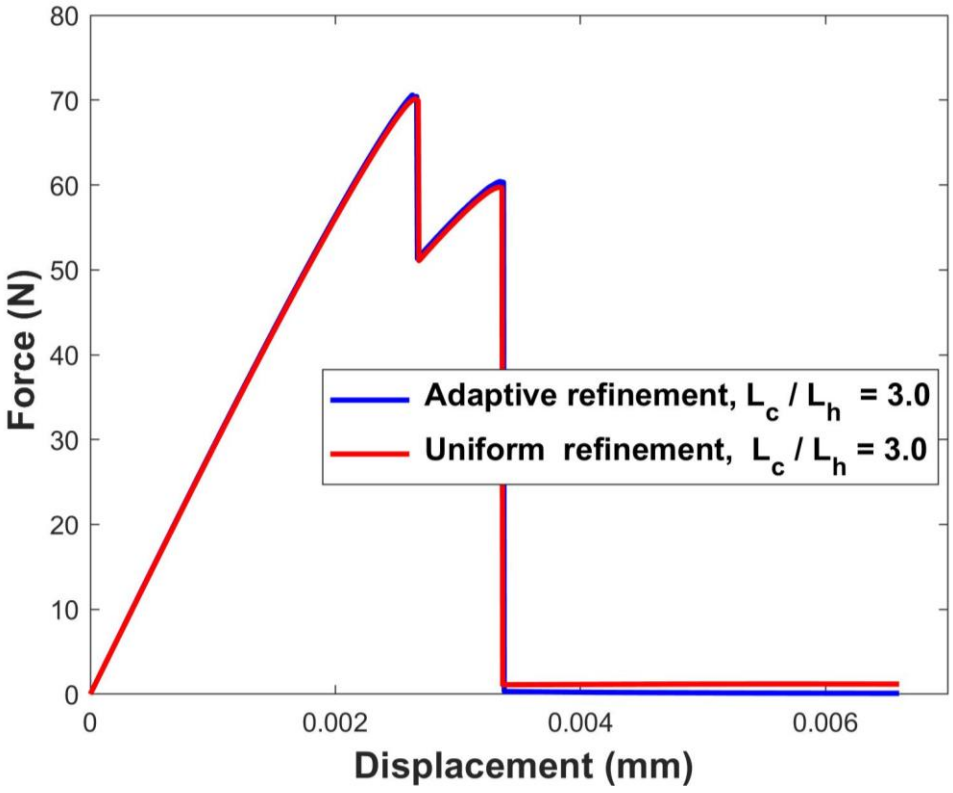

Fig. 35. Load-displacement curves obtained from the uniform refinement and the proposed method, respectively

Table 5

Computing time, number of DOFs and number of cells for the proposed method and the uniform refinement (Rock model including multiple fractures)

Methods	Computing time (h)	Number of DOFs	Number of cells

The proposed method	0.2472	9754	3484
Uniform refinement	11.4302	122412	40000

5. Conclusions

Rock fracture has important effects in geotechnical engineering, such as in blasting, oil and gas exploration, and rock landslides. Based on this, this study develops an adaptive isogeometric method of the fourth-order phase field model for simulating rock fracture using a novel refinement criterion and an improved data transfer operator (HBFT). (1) The proposed refinement criterion is easy to implement and reduces the number of computing cells. Additionally, it only requires a simple addition or subtraction operation on the 1D knot vector of the IGA for guaranteeing the hierarchical difference of adjacent cells; (2) The proposed HBFT only transfers the history variables in the local region to be refined, while keeping the variables in other regions unchanged; thus it reduces the transfer errors and the number of basis functions required in the intermediate steps. Besides, compared with the global and cell-by-cell versions in the traditional BFT, the proposed HBFT not only has the potential to avoid solving large-scale linear equations of the global version, but also alleviates, to a certian extent, the requirement of the cell-by-cell version for the full integration cell.

The results show that the proposed adaptive phase-field method decreases the calculation time and storage requirements by over 90% compared to the uniform

669 refinement in the most cases, and the calculation time of incorporating non-equal order
670 cells is 35.23% less than that of the equal order cells.

671 Notably, to reduce computing time, this paper pre-calculates and stores the basis
672 functions and their derivative values, and only updates the values in the region to be
673 refined during the adaptive analysis. However, it should be noted that only a
674 preliminary validation of HBFT has been performed in this paper. And its performance
675 in non-monotonic loading and other complex cases will be analyzed in authors' future
676 work.

Appendix A

```
function ij_marked_elems = ij_algorithm(marked_elems,active,deactivated,nel_dir)

    % Purpose:Compute the ij-marked area of level ilevel in the current local refinement

    % marked_elems: Cells marked for the current local refinement on level ilevel, i.e.,{Q ∈ Q_ilevel | Q ⊂ currentTime Ω^refined_ilevel }
    %       active: Active cells on level ilevel after the last local refinement, i.e., {Q ∈ lastTime Q | Q ⊂ lastTime Ω_ilevel ∧ Q ⊄ ⋃_{k=level+1}^{n} lastTime Ω_k}
    %  deactivated: deactivated cells on level ilevel after the last local refinement, i.e.,{Q ∈ lastTime Q | Q ⊂ lastTime Ω_ilevel ∧ Q ⊂ ⋃_{k=level-1}^{n} lastTime Ω_k}
    %      nel_dir: Number of cells in each direction

    % Subscripts
    [i,j] = ind2sub(nel_dir,marked_elems);%col vector

    % Scalar
    i_max = nel_dir(1);
    i_min = 1;

    j_max = nel_dir(2);
    j_min = 1;

    % Auxiliary subscripts
    i_minus1 = i-1;
    i_plus1 = i+1;

    j_minus1 = j-1;
    j_plus1 = j+1;

    % Remove the illegal number
    i_minus1_mask = i_minus1 <= i_max & i_minus1 >= i_min;
    i_plus1_mask = i_plus1 <= i_max & i_plus1 >= i_min;

    j_minus1_mask = j_minus1 <= j_max & j_minus1 >= j_min;
    j_plus1_mask = j_plus1 <= j_max & j_plus1 >= j_min;

    % Element set1, the combination of (i-1;j-1)
    elem_set1_ij_mask = i_minus1_mask & j_minus1_mask;
    % Element set2, the combination of (i-1;j)
    elem_set2_ij_mask = i_minus1_mask;
    % Element set3, the combination of (i-1;j+1)
    elem_set3_ij_mask = i_minus1_mask & j_plus1_mask;

    % Element set4, the combination of (i;j-1)
    elem_set4_ij_mask = j_minus1_mask;
    % Element set5, the combination of (i;j+1)
    elem_set5_ij_mask = j_plus1_mask;

    % Element set6, the combination of (i+1;j-1)
    elem_set6_ij_mask = i_plus1_mask & j_minus1_mask;
    % Element set7, the combination of (i+1;j)
    elem_set7_ij_mask = i_plus1_mask;
    % Element set8, the combination of (i+1;j+1)
    elem_set8_ij_mask = i_plus1_mask & j_plus1_mask;

    % The subscripts of elem_set 1-8
    elem_set1_i = i_minus1(elem_set1_ij_mask);
    elem_set1_j = j_minus1(elem_set1_ij_mask);

    elem_set2_i = i_minus1(elem_set2_ij_mask);
    elem_set2_j = j(elem_set2_ij_mask);

    elem_set3_i = i_minus1(elem_set3_ij_mask);
    elem_set3_j = j_plus1(elem_set3_ij_mask);

    elem_set4_i = i(elem_set4_ij_mask);
    elem_set4_j = j_minus1(elem_set4_ij_mask);

    elem_set5_i = i(elem_set5_ij_mask);
    elem_set5_j = j_plus1(elem_set5_ij_mask);

    elem_set6_i = i_plus1(elem_set6_ij_mask);
    elem_set6_j = j_minus1(elem_set6_ij_mask);

    elem_set7_i = i_plus1(elem_set7_ij_mask);
    elem_set7_j = j(elem_set7_ij_mask);

    elem_set8_i = i_plus1(elem_set8_ij_mask);
    elem_set8_j = j_plus1(elem_set8_ij_mask);

    % Linear indices
    elem_set1 = sub2ind(nel_dir,elem_set1_i,elem_set1_j);
    elem_set2 = sub2ind(nel_dir,elem_set2_i,elem_set2_j);
    elem_set3 = sub2ind(nel_dir,elem_set3_i,elem_set3_j);
    elem_set4 = sub2ind(nel_dir,elem_set4_i,elem_set4_j);
    elem_set5 = sub2ind(nel_dir,elem_set5_i,elem_set5_j);
    elem_set6 = sub2ind(nel_dir,elem_set6_i,elem_set6_j);
    elem_set7 = sub2ind(nel_dir,elem_set7_i,elem_set7_j);
    elem_set8 = sub2ind(nel_dir,elem_set8_i,elem_set8_j);

    % Remove the duplicate elements
    elem_set1_4 = [elem_set1;elem_set2;elem_set3;elem_set4];
    elem_set5_8 = [elem_set5;elem_set6;elem_set7;elem_set8];
    elem_set = union(elem_set1_4,elem_set5_8);% col vector


    % The elements in the ij_marked_area
    inner_elements = union(active,deactivated);% col vector

    ij_marked_elems = setdiff(elem_set,inner_elements);% col vector

end
```

Fig. 36. Matlab source codes of the *i-j algorithm*

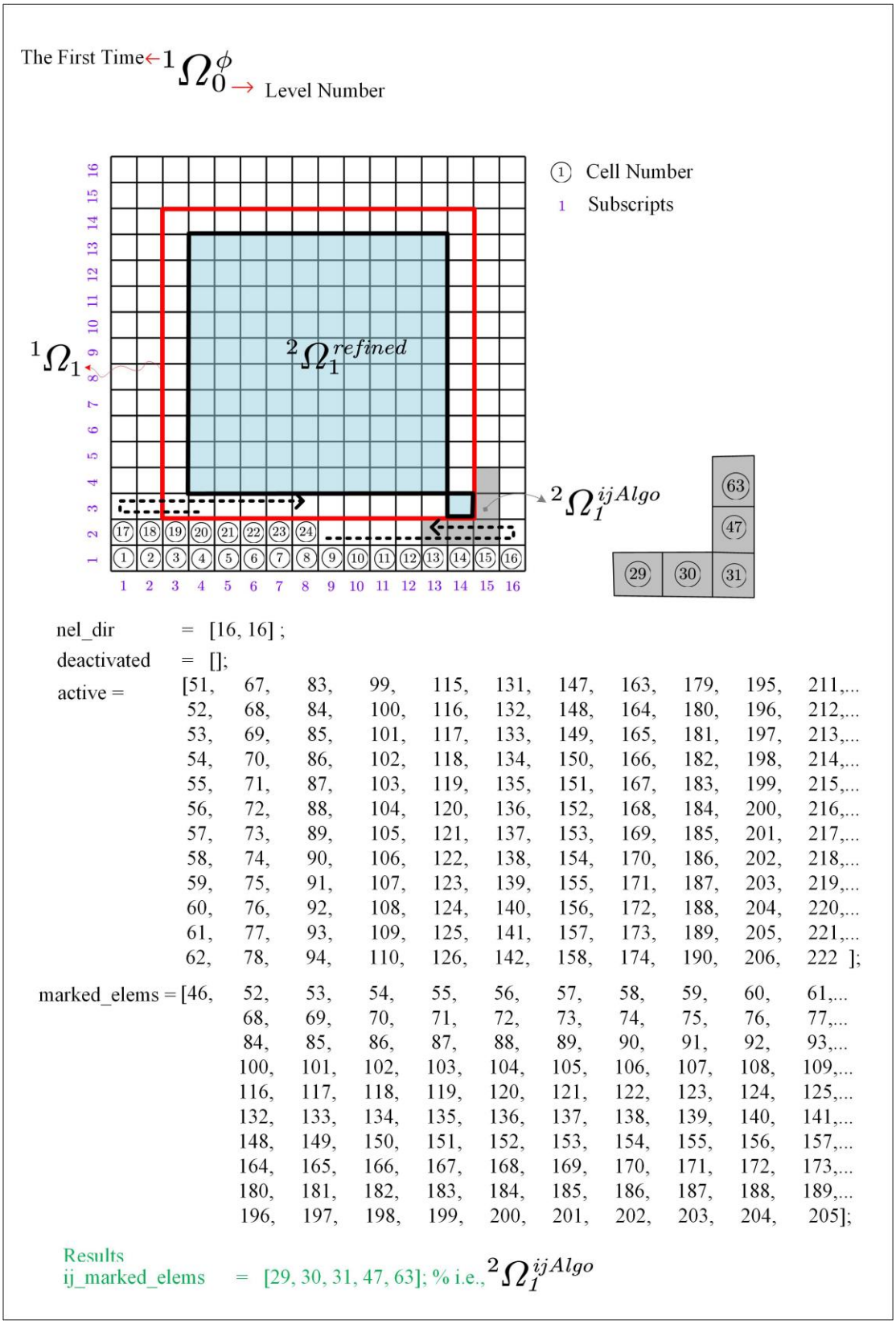

Fig. 37. A simple example for illustrating the *i-j algorithm*: solving the ij-marked area ${}^{2}\Omega_{1}^{ijAlgo}$ of level 2 in the second local refinement in Fig.5.

Acknowledgement

The work is supported by the National Natural Science Foundation of China (Nos. 51979025 and 52011530189).

Reference

Aimene, Y., Hammerquist, C., Ouenes, A., 2019. Anisotropic damage mechanics for asymmetric hydraulic fracture height propagation in a layered unconventional gas reservoir. J. Nat. Gas Sci. Eng. 67, 1–13. https://doi.org/10.1016/j.jngse.2019.04.013

Ambati, M., Gerasimov, T., De Lorenzis, L., 2014. A review on phase-field models of brittle fracture and a new fast hybrid formulation. Comput. Mech. 55, 383–405. https://doi.org/10.1007/s00466-014-1109-y

Borden, M.J., Hughes, T.J.R., Landis, C.M., Verhoosel, C. V., 2014. A higher-order phase-field model for brittle fracture: Formulation and analysis within the isogeometric analysis framework. Comput. Methods Appl. Mech. Eng. 273, 100–118. https://doi.org/10.1016/j.cma.2014.01.016

Bornemann, P.B., Cirak, F., 2013. A subdivision-based implementation of the hierarchical b-spline finite element method. Comput. Methods Appl. Mech. Eng. 253, 584–598. https://doi.org/10.1016/j.cma.2012.06.023

Bourdin, B., Francfort, G.A., Marigo, J.J., 2000. Numerical experiments in revisited brittle fracture. J. Mech. Phys. Solids 48, 797–826. https://doi.org/10.1016/S0022-5096(99)00028-9

Buffa, A., Garau, E.M., 2017. Refinable spaces and local approximation estimates for hierarchical splines. IMA J. Numer. Anal. 37, 1125–1149. https://doi.org/10.1093/imanum/drw035

703 Camones, L.A.M., Vargas, E. do A., de Figueiredo, R.P., Velloso, R.Q., 2013. Application of the
704 discrete element method for modeling of rock crack propagation and coalescence in the step-path
705 failure mechanism. Eng. Geol. 153, 80–94. https://doi.org/10.1016/j.enggeo.2012.11.013
706 Cheng, Z., Gong, W., Tang, H., Juang, C.H., Deng, Q., Chen, J., Ye, X., 2021. UAV photogrammetry-
707 based remote sensing and preliminary assessment of the behavior of a landslide in Guizhou,
708 China. Eng. Geol. 289, 106172. https://doi.org/10.1016/j.enggeo.2021.106172
709 Cruz, F., Roehl, D., Vargas, E. do A., 2019. An XFEM implementation in Abaqus to model
710 intersections between fractures in porous rocks. Comput. Geotech. 112, 135–146.
711 https://doi.org/10.1016/j.compgeo.2019.04.014
712 Cruz, F., Roehl, D., Vargas, E. do A., 2018. An XFEM element to model intersections between
713 hydraulic and natural fractures in porous rocks. Int. J. Rock Mech. Min. Sci. 112, 385–397.
714 https://doi.org/10.1016/j.ijrmms.2018.10.001
715 Fei, F., Choo, J., 2020. A phase-field model of frictional shear fracture in geologic materials. Comput.
716 Methods Appl. Mech. Eng. 369, 113265. https://doi.org/10.1016/j.cma.2020.113265
717 Garau, E.M., Vázquez, R., 2018. Algorithms for the implementation of adaptive isogeometric methods
718 using hierarchical B-splines. Appl. Numer. Math. https://doi.org/10.1016/j.apnum.2017.08.006
719 Gaume, J., Van Herwijnen, A., Chambon, G., Birkeland, K.W., Schweizer, J., 2015. Modeling of crack
720 propagation in weak snowpack layers using the discrete element method. Cryosphere 9, 1915–
721 1932. https://doi.org/10.5194/tc-9-1915-2015
722 Giannelli, C., Jüttler, B., Speleers, H., 2014. Strongly stable bases for adaptively refined multilevel
723 spline spaces. Adv. Comput. Math. 40, 459–490. https://doi.org/10.1007/s10444-013-9315-2

Giannelli, C., Jüttler, B., Speleers, H., 2012. THB-splines: The truncated basis for hierarchical splines. Comput. Aided Geom. Des. 29, 485–498. https://doi.org/10.1016/j.cagd.2012.03.025

Gong, W., Juang, C.H., Wasowski, J., 2021. Geohazards and human settlements: Lessons learned from multiple relocation events in Badong, China – Engineering geologist's perspective. Eng. Geol. 285, 106051. https://doi.org/10.1016/j.enggeo.2021.106051

Goswami, S., Anitescu, C., Chakraborty, S., Rabczuk, T., 2020a. Transfer learning enhanced physics informed neural network for phase-field modeling of fracture. Theor. Appl. Fract. Mech. 106, 102447. https://doi.org/10.1016/j.tafmec.2019.102447

Goswami, S., Anitescu, C., Rabczuk, T., 2020b. Adaptive fourth-order phase field analysis for brittle fracture. Comput. Methods Appl. Mech. Eng. 361, 112808. https://doi.org/10.1016/j.cma.2019.112808

Goswami, S., Anitescu, C., Rabczuk, T., 2019. Adaptive phase field analysis with dual hierarchical meshes for brittle fracture. Eng. Fract. Mech. 218, 106608. https://doi.org/10.1016/j.engfracmech.2019.106608

Hennig, P., Ambati, M., De Lorenzis, L., Kästner, M., 2018. Projection and transfer operators in adaptive isogeometric analysis with hierarchical B-splines. Comput. Methods Appl. Mech. Eng. 334, 313–336. https://doi.org/10.1016/j.cma.2018.01.017

Hennig, P., Müller, S., Kästner, M., 2016. Bézier extraction and adaptive refinement of truncated hierarchical NURBS. Comput. Methods Appl. Mech. Eng. https://doi.org/10.1016/j.cma.2016.03.009

744 Hirshikesh, H., Pramod, A.L.N., Waisman, H., Natarajan, S., 2021. Adaptive phase field method using
745 novel physics based refinement criteria. Comput. Methods Appl. Mech. Eng. 383, 113874.
746 https://doi.org/10.1016/j.cma.2021.113874
747 Hu, Z., Zhang, H., Zheng, Y., Ye, H., 2022. Phase-field implicit material point method with the
748 convected particle domain interpolation for brittle – ductile failure transition in geomaterials
749 involving finite deformation. Comput. Methods Appl. Mech. Eng. 390, 114420.
750 https://doi.org/10.1016/j.cma.2021.114420
751 Li, Fu, Z., Wang, Y., Tang, H., Yan, J., Gong, W., Yao, W., Criss, R.E., 2019. Susceptibility of
752 reservoir-induced landslides and strategies for increasing the slope stability in the Three Gorges
753 Reservoir Area : Zigui Basin as an example. Eng. Geol. 261, 105279.
754 https://doi.org/10.1016/j.enggeo.2019.105279
755 Li, Y., Yu, T., Natarajan, S., 2022. An adaptive isogeometric phase-field method for brittle fracture in
756 rock-like materials. Eng. Fract. Mech. 263, 108298.
757 https://doi.org/10.1016/j.engfracmech.2022.108298
758 Miehe, C., Hofacker, M., Welschinger, F., 2010. A phase field model for rate-independent crack
759 propagation: Robust algorithmic implementation based on operator splits. Comput. Methods
760 Appl. Mech. Eng. 199, 2765–2778. https://doi.org/10.1016/j.cma.2010.04.011
761 Oterkus, S., Madenci, E., Oterkus, E., 2017. Fully coupled poroelastic peridynamic formulation for
762 fluid-filled fractures. Eng. Geol. 225, 19–28. https://doi.org/10.1016/j.enggeo.2017.02.001
763 Rabczuk, T., Ren, H., 2017. A peridynamics formulation for quasi-static fracture and contact in rock.
764 Eng. Geol. 225, 42–48. https://doi.org/10.1016/j.enggeo.2017.05.001
765 Ren, H., 2021. Dual-horizon peridynamics and nonlocal operator method.

766 Ren, H., Zhuang, X., Cai, Y., Rabczuk, T., 2016. Dual-horizon peridynamics. Int. J. Numer. Methods
767 Eng. 108, 1451–1476. https://doi.org/10.1002/nme.5257
768 Ren, H., Zhuang, X., Rabczuk, T., 2017. Dual-horizon peridynamics: A stable solution to varying
769 horizons. Comput. Methods Appl. Mech. Eng. 318, 762–782.
770 https://doi.org/10.1016/j.cma.2016.12.031
771 Samaniego, C., Ulloa, J., Rodríguez, P., Houzeaux, G., Vázquez, M., Samaniego, E., 2021. A phase-
772 field model for ductile fracture with shear bands: A parallel implementation. Int. J. Mech. Sci.
773 200, 106424. https://doi.org/10.1016/j.ijmecsci.2021.106424
774 Schillinger, D., Dedè, L., Scott, M.A., Evans, J.A., Borden, M.J., Rank, E., Hughes, T.J.R., 2012. An
775 isogeometric design-through-analysis methodology based on adaptive hierarchical refinement of
776 NURBS, immersed boundary methods, and T-spline CAD surfaces. Comput. Methods Appl.
777 Mech. Eng. 249–252, 116–150. https://doi.org/10.1016/j.cma.2012.03.017
778 Song, X., Silling, S.A., 2020. On the peridynamic effective force state and multiphase constitutive
779 correspondence principle. J. Mech. Phys. Solids 145, 104161.
780 https://doi.org/10.1016/j.jmps.2020.104161
781 Spetz, A., Denzer, R., Tudisco, E., Dahlblom, O., 2021. A Modified Phase-Field Fracture Model for
782 Simulation of Mixed Mode Brittle Fractures and Compressive Cracks in Porous Rock. Rock
783 Mech. Rock Eng. 54, 5375–5388. https://doi.org/10.1007/s00603-021-02627-4
784 van derBeek, P., 2021. Stressed rocks cause big landslides. Nat. Geosci. 14, 261–262.
785 https://doi.org/10.1038/s41561-021-00748-7

786 Vuong, A. V., Giannelli, C., Jüttler, B., Simeon, B., 2011. A hierarchical approach to adaptive local
787 refinement in isogeometric analysis. Comput. Methods Appl. Mech. Eng. 200, 3554–3567.
788 https://doi.org/10.1016/j.cma.2011.09.004
789 Wu, J., Nguyen, V.P., Nguyen, C.T., Sutula, D., Sinaie, S., 2019. Phase-field modelling of fracture.
790 Zhou, S., Zhuang, X., Rabczuk, T., 2018a. A phase-field modeling approach of fracture propagation in
791 poroelastic media. Eng. Geol. 240, 189–203. https://doi.org/10.1016/j.enggeo.2018.04.008
792 Zhou, S., Zhuang, X., Zhu, H., Rabczuk, T., 2018b. Phase field modelling of crack propagation,
793 branching and coalescence in rocks. Theor. Appl. Fract. Mech. 96, 174–192.
794 https://doi.org/10.1016/j.tafmec.2018.04.011
795 Zhou, X., Wang, L., Shou, Y., 2020. Understanding the fracture mechanism of ring Brazilian disc
796 specimens by the phase field method. Int. J. Fract. 226, 17–43. https://doi.org/10.1007/s10704-
797 020-00476-w
798 Zhu, F., Tang, H., Zhang, X., Papazafeiropoulos, G., 2022. Fourth-order hybrid phase field analysis
799 with non-equal order elements and dual meshes for simulating crack propagation. Comput.
800 Geotech. 142, 104587. https://doi.org/10.1016/j.compgeo.2021.104587
801 Zhu, F., Zhao, J., 2021. Peridynamic modelling of blasting induced rock fractures. J. Mech. Phys.
802 Solids 153, 104469. https://doi.org/10.1016/j.jmps.2021.104469
803 Zhuang, X., Augarde, C.E., Mathisen, K.M., 2012. Fracture modeling using meshless methods and
804 level sets in 3D : Framework and modeling. https://doi.org/10.1002/nme
805 Zhuang, X., Zhu, H., Augarde, C., 2014. An improved meshless Shepard and least squares method
806 possessing the delta property and requiring no singular weight function 343–357.
807 https://doi.org/10.1007/s00466-013-0912-1